

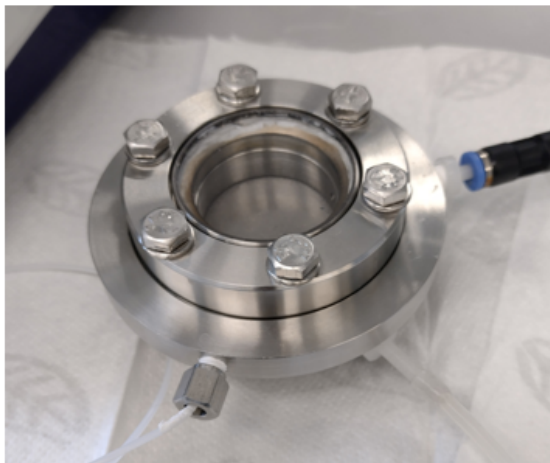
---

# Fabrication of Photocatalytic 2D/TiO<sub>2</sub> Membranes for Phenol Abatement and Separation

---

Chemical Engineering & Chemistry: Master thesis

Submitted June 01, 2023



Martin Brandstrup Olesen

**Title:**

Fabrication of Photocatalytic 2D/TiO<sub>2</sub> Membranes for Phenol Abatement and Separation

**Theme:**

Membrane filtration

**Project period:**

September 01, 2022 to June 01, 2023

**Author:**

Martin Brandstrup Olesen

**Supervisor(s):**

Vittorio Boffa

**Number of pages:**

48 pages

**Submission date:**

June 01, 2023

**Abstract**

This project concerns the synthesis and usage of 2D materials to produce photocatalytic membranes for phenol abatement and separation. MXene and MnO<sub>2</sub> nanosheets were synthesized and characterized by XRD, showing similar diffractograms as found by others. Commercially acquired graphene oxide (GO) and TiO<sub>2</sub> were characterized by XRD as well. Photocatalytic degradation of phenol was investigated using dispersions of GO, MXene, MnO<sub>2</sub> and TiO<sub>2</sub> as catalysts. Only TiO<sub>2</sub> showed photocatalytic properties. Similar degradation experiments showed that GO had better synergy with TiO<sub>2</sub> than MXene and MnO<sub>2</sub>. Membranes were produced by vacuum filtration using either cellulose acetate, nylon or PVDF filter as support membrane and using GO, MXene, MnO<sub>2</sub> and TiO<sub>2</sub> as the active layer. The use of PVDF resulted in the best adherence of active layer. Membranes containing TiO<sub>2</sub> in the active layer showed photocatalytic properties, but failed to reject phenol during filtration. Using only GO or MXene as the active layer yielded phenol rejections at 7.5% and 29.9%, respectively. The obtained water flux was 5.06Lm<sup>-2</sup>bar<sup>-1</sup>h<sup>-1</sup> for the GO membrane and 0.75Lm<sup>-2</sup>bar<sup>-1</sup>h<sup>-1</sup> for the MXene membrane.

# Foreword

This project is written in the autumn semester 2022 and spring semester 2023 and constitutes the final thesis for the master's degree "Master of Science (MSc) in Engineering (Chemistry)" at Aalborg University.

The author thanks project supervisor Vittorio Boffa for his guidance, ideas and resources throughout the whole project period. Moreover, the author thanks Wachirapun Punkrawee for his collaboration in synthesizing manganese oxide nanosheets. The author also thanks Jingbo Ni for his efforts in synthesizing MXene.

## Abbreviations

The following abbreviations are used throughout the report:

Abbreviation	Meaning
GO	Graphene Oxide
PVDF	Polyvinyledene fluoride
TMA·OH	Tetramethylammonium hydroxide
XRD	X-Ray diffraction
HPLC	High Pressure Liquid Chromatography
UV	Ultra violet
DI-water	Deionized water

# Contents

<b>1</b>	<b>Introduction</b>	<b>1</b>
<b>2</b>	<b>Theory</b>	<b>3</b>
2.1	Photocatalysis .....	3
2.1.1	Photocatalytic degradation of phenol .....	4
2.2	2D materials.....	6
2.2.1	Graphene oxide .....	7
2.2.2	MnO <sub>2</sub> nanosheets .....	8
2.2.3	MXene nanosheets .....	8
2.3	2D membranes .....	9
2.3.1	Fabrication methods.....	11
<b>3</b>	<b>Materials &amp; methods</b>	<b>14</b>
3.1	Materials.....	14
3.1.1	Synthesis of MnO <sub>2</sub> -nanosheets.....	14
3.1.2	Synthesis of Ti <sub>3</sub> C <sub>2</sub> T <sub>x</sub> MXene.....	15
3.1.3	2D material attached to TiO <sub>2</sub> .....	15
3.2	Membrane fabrication .....	16
3.3	Photocatalytic testing of dispersions .....	16
3.4	Membrane filtration system.....	17
3.4.1	Photocatalytic testing of membranes.....	19
3.4.2	Membrane filtration .....	19
<b>4</b>	<b>Results &amp; Discussion</b>	<b>21</b>
4.1	Characterization of materials.....	21
4.1.1	XRD phase analysis .....	21
4.2	Photocatalytic performance of dispersions.....	22
4.3	Membrane characterization .....	26
4.3.1	XRD analysis of membranes and supports .....	27
4.3.2	Contact angle.....	29
4.4	Membrane performance .....	31
4.4.1	Photocatalytic degradation .....	31
4.4.2	Permeation and selectivity .....	33
<b>5</b>	<b>Conclusion</b>	<b>35</b>
	<b>Bibliography</b>	<b>36</b>
	<b>Appendix</b>	<b>42</b>

A	Appendix 1 .....	43
---	------------------	----

# 1 Introduction

Hundreds of millions of people currently lack access to clean drinking water, making the accessibility a major global concern.[1][2]. Moreover, polluted wastewater causes major environmental issues due to their harmful effects to various ecosystems [3]. One common and concerning pollutant is phenol, which is toxic at low concentrations and has a low biodegradability [4][5]. Phenol is released to the environment as a waste product from various industries such as refineries, petrochemical plants, pharmaceuticals, plastics and paints. Both soil and groundwater is contaminated when phenol is released to the environment. Thus, processes or treatments to remove phenol from wastewater are required to minimize the environmental damages caused by discharging the wastewater [6][5].

Multiple methods and techniques have been used to remove phenol from wastewater. These are commonly separated into three categories; chemical and biological removal and physical separation [7][8]. Chemical removal uses additive compounds, such as Fenton reagents or ozone, to remove phenol by chemical reactions, but can in some cases result in the formation of non-biodegradable and toxic byproducts [9]. Phenol removal by biological means are often less effective compared to chemical removal, as the biological processes tend to occur at a slower pace [3]. Physical separation by membrane filtration has on the other hand shown promising results without any noteworthy downsides [10]. Membrane filtration can produce clean water of high quality and at a high capacity without use of additives [8]. However, traditional membrane filtration does not abate phenol, but rather draws clean water from the wastewater, thus increasing the concentration of any pollutants in the retentate stream.

Polymeric membranes are the dominating choice in the membrane separation industry, as they provide good processability, easy usage and good separation performance while being cost-effective [11]. However, polymeric membranes usually have an intrinsic trade-off between permeation and selectivity. A highly selective polymeric membrane will often have a low permeation, while a low selective membrane will have high permeation [12]. The use of 2D materials can be the key to surpass this trade-off [11][13]. 2D materials are sheet materials, having a thickness of only one or few atoms and a large lateral size. This sheet structure makes 2D materials depositable as ultra-thin layers and the pore structure is, in many cases, highly controllable. Large pores promotes a high permeation, whereas small pores promote a high selectivity. Moreover, water permeation is inversely proportional to membrane thickness [14]. By depositing an ultra-thin layer of 2D material

with an appropriate pore size for the targeted pollutant, it is possible to produce a membrane that overcome the aforementioned intrinsic trade-off [15]. One of the most well-known 2D materials used for membrane application is graphene oxide, which has shown great potential in the field of membrane separation. In addition, graphene oxide membranes have great mechanical properties, such as high strength and flexibility, and also exhibits a high chemical resistance. However, the search for new 2D materials persists and other promising 2D materials have emerged, such as MXenes, MoS<sub>2</sub>, metal organic frameworks and others [14].

Recently, membrane filtration have been subjected to an additional functionality, as the use of catalytic materials in a membrane-setting has been explored [16]. These membranes can both abate pollutants by catalytic degradation and separate them physically. Catalytic membranes use either thermal or photon energy to degrade pollutants in the wastewater stream, while simultaneously producing clean water by membrane filtration [17]. Ultimately, this causes the catalytic membrane to yield cleaner water in both retentate and permeate. In addition, the catalytic function can in some cases help to reduce fouling of the membrane. Pollutant molecules near the active layer of the membrane will undergo degradation and thereby reduce the size of the fouling layer that occurs at the membrane surface [16].

Catalytic membranes usually consist of two or more components, where each component gives a specific function to the membrane. For instance, a photocatalytic membrane consisting of 2D graphene oxide and TiO<sub>2</sub> particles is utilising the sieve-like property from graphene oxide to reject pollutant molecules, while TiO<sub>2</sub> particles enables photocatalytic degradation of the pollutant, when exposed to light of an appropriate wavelength [16].

In this work, photocatalytic membranes consisting of graphene oxide, MXene, MnO<sub>2</sub>-nanosheets and TiO<sub>2</sub> will be fabricated by vacuum filtration. The goal is to investigate these materials separately and in membrane application. In addition, these photocatalytic membranes will be evaluated in regards to their abilities to degrade and separate phenol. In a larger perspective, this could help in the design of future photocatalytic 2D membranes.

## 2 Theory

### 2.1 Photocatalysis

Photocatalysis is a phenomenon where photon energy, in combination with a photocatalyst, is used to drive a chemical reaction [18]. Two types of photocatalyses exist; either homogeneous or heterogeneous. Homogeneous photocatalysis refers to the catalyst and reactant existing in the same phase, whereas heterogeneous photocatalysis refers to a reaction between two separate phases. In the case of water purification, heterogeneous photocatalysis is often utilized by having a solid catalyst, such as  $\text{TiO}_2$  and a aqueous reactant, such as pollutants dissolved in wastewater [19][18]. Solid photocatalysts for water purification are always semiconductors, often transition metal oxides, that can absorb photon energy which results in excitation of electrons and the simultaneous formation of electron holes. Semiconductors have void energy regions where no energy levels are appropriate for the recombination of the electron-hole pairs. The void energy region is the difference between the energy levels of the valence and conduction bands, also known as the band-gap [20]. The band-gap of the photocatalyst needs to be equal to or lower than the energy of the received photon to form electron-hole pairs [18]. The excited electron and electron hole are reductive and oxidative, respectively, and these species can either recombine or migrate to the surface of the photocatalyst. Migration to photocatalyst surface will in aqueous conditions result in formation of reactive oxygen species, such as  $\text{O}_2^-$  and  $\text{OH}^\bullet$ .  $\text{O}_2^-$  is formed from dissolved  $\text{O}_2$  being reduced by an excited electron from the conduction band and  $\text{OH}^\bullet$  is formed from  $\text{OH}^-$  being oxidized from the electron hole in the valence band. These radicals will react with organic pollutants causing them to undergo degradation. Another option for degradation is a direct reduction or oxidation by the excited electron or electron hole when the organic pollutant is adsorbed on the catalyst surface [21].

For  $\text{TiO}_2$ , as shown in Figure 2.1, the band-gap is equal to 3.2 eV corresponding to light with a wavelength of 387.5 nm (converted by Planck's energy equation). This means that  $\text{TiO}_2$  can become photo activated by regular sunlight, as a portion of sunlight is equal to or higher energy than the band-gap energy.

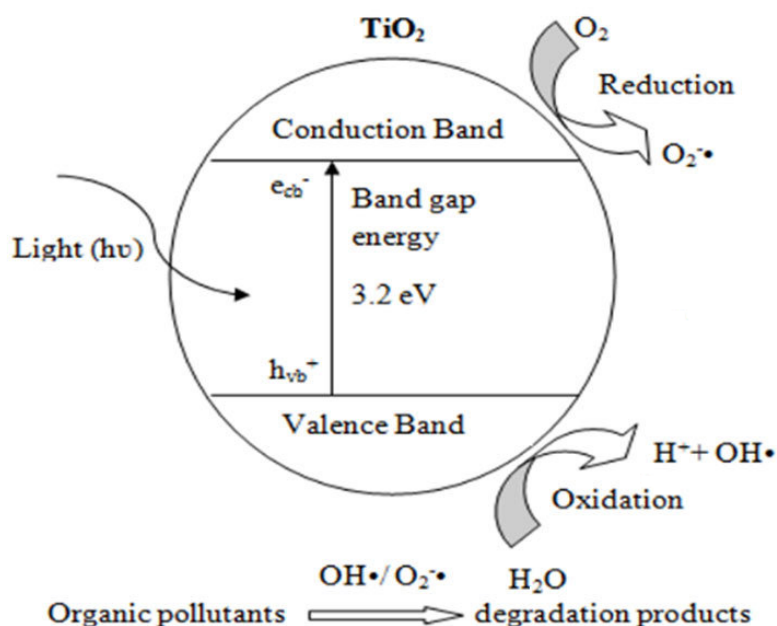


Figure 2.1: Photocatalysis for  $\text{TiO}_2$  particle in aqueous medium. Modified from [20].

### 2.1.1 Photocatalytic degradation of phenol

Degradation of phenol by photocatalysis involves the formation of multiple intermediates before complete mineralization of phenol is achieved. The degradation reaction takes place between the radicals formed by photocatalysis and the phenol molecule. Here the electrophilic  $\text{OH}^{\bullet}$ -radical attacks the electron-rich ortho or para carbon atoms, leading to the formation of dihydroxycyclohexadienyl (DCHD). Subsequently, DCHD undergoes further reactions with dissolved  $\text{O}_2$  to yield dihydroxy benzenes and  $^{\bullet}\text{HO}_2$  radicals, before being completely mineralized to  $\text{CO}_2$  and  $\text{H}_2\text{O}$  [22]. The degradation process has several influencing parameters such as light intensity, phenol concentration, catalyst concentration, presence of oxidizing agents/electron donors and solution pH [23].

Light intensity has been reported to have an either linear or square root dependency on the degradation reaction. Ollis and Pelizzetti [24] found that the degradation rate for organic pollutants is proportional to the radiant flux up to a certain threshold. Exceeding the threshold causes the degradation rate to follow the square root of the radiant flux instead e.g. a lower photocatalytic

efficiency.

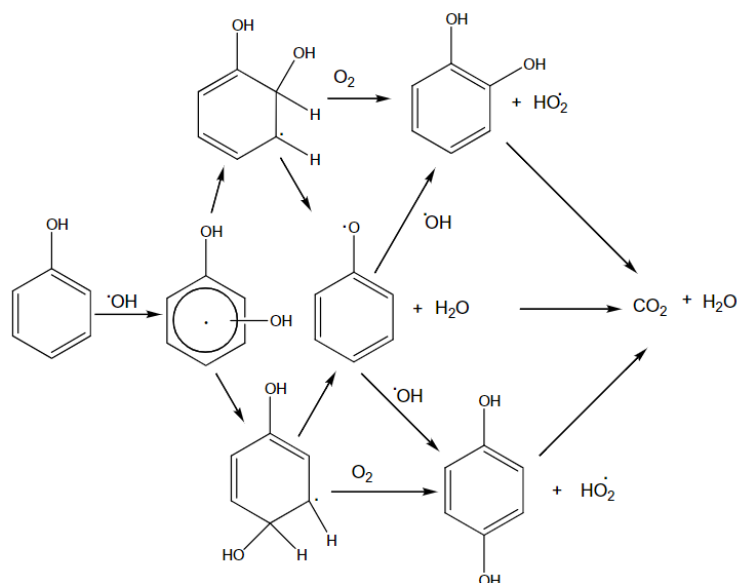


**Figure 2.2:** Degradation path for phenol during photocatalysis [22].

The concentration of phenol has shown to affect the degradation rate, with the tendency of a low phenol concentration promoting a higher percentage-wise degradation. Adsorption on catalyst surface increases at higher phenol concentration and the amount of radicals needed for degradation increases proportionally. However, the production of radicals is not related to the amount of adsorbed species, which means that the relative number of formed radicals/adsorbed species decreases and results in a decreased degradation percentage. [21].

Catalyst concentration is another parameter that has great influence on the process. Higher amount of catalyst gives more sites for phenol adsorption and more sites for light harvesting which should promote phenol adsorption and radical formation, both leading to faster degradation. However, this is not the case due to several solution factors. Two of the factors are light scattering and screening that occurs if the solution contains too many particles [21]. A too large amount of particles will screen off the incoming light and scatter it, causing the amount of harvested light to decrease. In addition, particle-to-particle interactions become more relevant at higher catalyst concentrations and agglomeration is more likely to occur. Agglomeration of catalyst particles reduces the active surface area and number of adsorption sites, yielding a lower catalytic efficiency. The amount of

catalyst is subjected to a trade off between the rate increasing factors and the rate decreasing factors. An optimum catalyst concentration can be found experimentally as it is also heavily based on the experimental setup and conditions [25].

Presence of electron donor and acceptors plays a crucial role for the electron-hole recombination rate. Recombination is predominant if no suitable donor or acceptor is present in the solution. The general electron acceptor in heterogeneous photocatalysis is molecular oxygen, but is not restricted to oxygen, as other oxidative species have shown greater impact on the radical generation rate and thereby increasing degradation rate as well. For instance,  $H_2O_2$  have shown to increase the hydroxyl generation for  $TiO_2$  particles leading to a higher degree of degradation [26].

Solution pH is another key parameter to control during photocatalysis. The pH of wastewaters varies greatly and affects the dissolved species in regards to their protonation-state, solubility and hydrophilicity. Some pollutants are more stable if they are present in a certain protonation-state [26]. The catalyst is also greatly affected by solution pH as it affects the surface charge and the size of formed agglomerates, which is directly related to the catalyst's ability to adsorb organic molecules [21]. The optimal pH level for photocatalysis is highly depending on the system and will vary based on the present conditions. For the case of photocatalytic degradation of phenol using  $TiO_2$  as catalyst, Yuan et al. [27] reported that the optimal pH ranges were between 3-4 and 13-14.

## 2.2 2D materials

2D materials refer to a material where the crystalline lattice consists of a single or few layers of atoms. These materials exist in nature, for example certain clay minerals, but are often synthesised to obtain element specific materials. Several synthesis methods are reported in literature, but two approaches are mainly used; top-down exfoliation or bottom-up synthesis [28]. Top-down exfoliation involves the exfoliation of a layered material into a single sheet material by various exfoliation methods. This is the case for the synthesis of graphene oxide by Hummer's method, where the parent graphite is broken into single sheets by exfoliation processes [29]. The bottom-up synthesis does not involve an already existing material, but instead forms the material from precursors, for example by chemical vapor deposition [28].

### 2.2.1 Graphene oxide

Graphene oxide (GO) is one of the most well known and well researched 2D materials with a broad range of application. GO has a one-atom-thick sheet structure with surface functional groups such as epoxy, hydroxyl and carboxyl groups, as shown in Figure 2.3. The hydrophilic nature of the surface groups makes GO easy to disperse in aqueous solution. However, the abundance and type of surface groups can be altered by various means. For example, GO can be reduced chemically or thermally to remove residual oxygen surface groups [30].

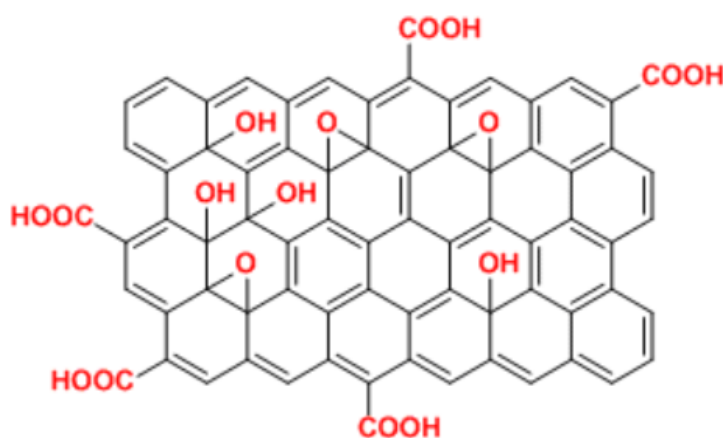


**Figure 2.3:** Representative structure of GO. The amount of surface groups varies based on the chosen synthesis method.

GO is often synthesized by Hummer's method [29] in which graphite is exposed to strong oxidation reactions, ultimately breaking the graphite into single graphene oxide sheets. The method involves the use of  $\text{KMnO}_4$  and  $\text{NaNO}_3$  dissolved in concentrated  $\text{H}_2\text{SO}_4$  as oxidation agent and will result in exfoliation of graphite within a few hours [29]. The original method has several flaws such as low yield and formation of toxic gasses, and has been subjected to several improvements since its discovery. For example, the use of  $\text{NaNO}_3$  has been removed in some syntheses and instead been replaced with a pre-oxidation step. Another example is an increase in the amount of  $\text{KMnO}_4$  and  $\text{H}_2\text{SO}_4$ . These improvements have resulted in a better synthesis route in terms of yield and safety concerns [31] [32].

### 2.2.2 MnO<sub>2</sub> nanosheets

MnO<sub>2</sub> nanosheets is a 2D material composed of a layer of manganese atoms sitting in the octahedral cavities between two layers of oxygen atoms, where each Mn-atom is coordinated to six O-atoms [33]. MnO<sub>2</sub>-nanosheets have several special features such as a broad absorption spectrum, negatively charged surface, good adsorption properties and degradation ability towards certain organic molecules. The use of MnO<sub>2</sub>-nanosheets has seen great interest in the field of biosensing and biomedicine, due to the special features that MnO<sub>2</sub>-nanosheet exhibits. In addition, MnO<sub>2</sub> can undergo degradation in the presence of oxidants, as Mn<sup>4+</sup> is an intermediate valence state of Mn, making the material suited for drug transport [34].

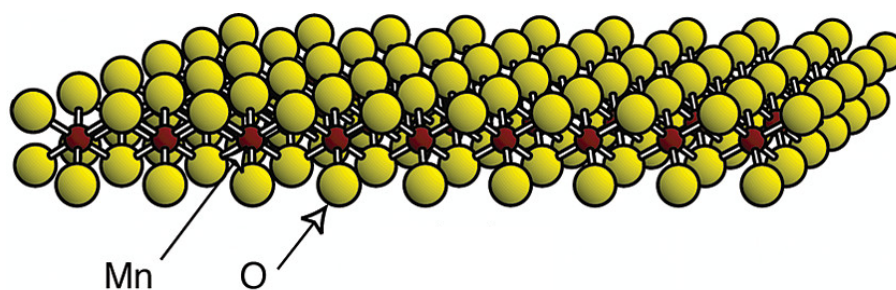


**Figure 2.4:** Structure of a single MnO<sub>2</sub> sheet composed of one manganese layer and two oxygen layers [33].

### 2.2.3 MXene nanosheets

MXene is a relatively new type of 2D material, which has shown promising properties in relation to membrane application [35]. MXene is a family name for materials that can be expressed as M<sub>n+1</sub>X<sub>n</sub>T<sub>x</sub>, where n can range from 1-3, M represents an early transition metal (Cr, Nb, Ti, V, etc.), X represents either carbon or nitrogen and T<sub>x</sub> refers to functional groups, usually =O, -OH and -F. The surface groups originate from the synthesis method where a direct or in-situ HF solution is usually used to selectively etch the A layer of an existing MAX-phase material. The A-layer in a MAX-phase material refers to a group of elements such as Al, Si, Sn, amongst others [36].

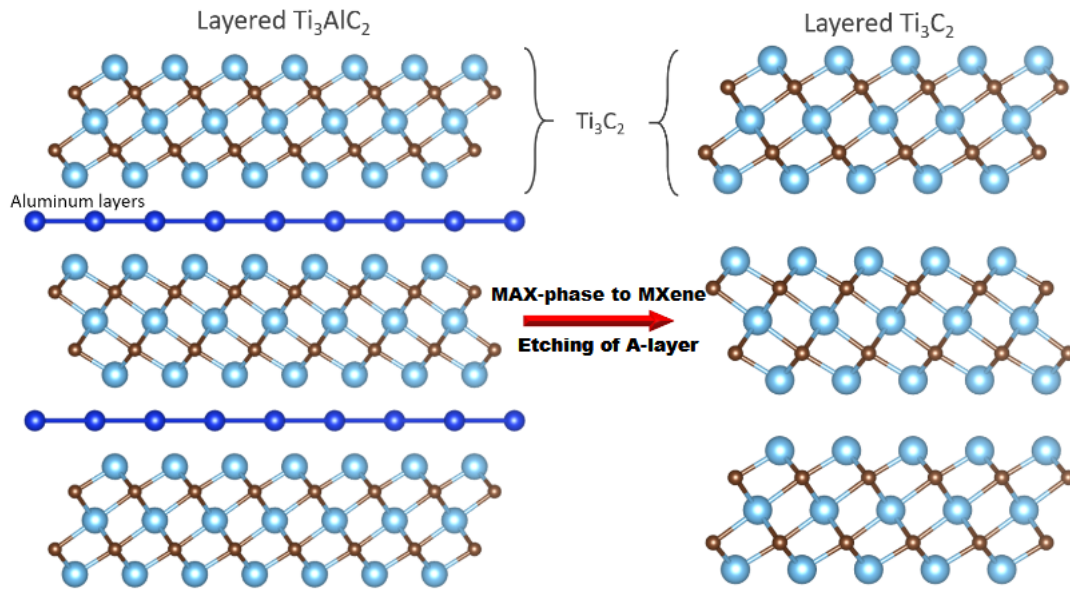


**Figure 2.5:** Structural model of MAX-phase and MXene for  $\text{Ti}_3\text{AlC}_2$ . Modified from [37].

In relation to membrane applications, MXenes have shown good properties such as excellent mechanical flexibility, thermal stability and antibacterial properties. In addition, both experimental and theoretical studies have shown that MXenes has great potential for fabricating high-flux and highly selective membranes [38]. Furthermore, MXenes has superior anti-swelling properties compared to GO if intercalated, due to the high abundance of surface groups found in MXenes. The surface groups promote a strong interaction between the intercalated ions and MXene sheets, thus reducing ion exchange and hydration of the interlayer ions [35].

## 2.3 2D membranes

2D materials used for membrane application provides the membrane with two main mechanisms of separation. One of the mechanisms is physical exclusion of molecules which is directly related to the pore size of the material. Generally, two types of nanopores are found in 2D materials, either nanoholes going through the 2D sheets or nanopores between the sheets e.g. the interlayer space [11]. Figure 2.6 illustrates a 2D membrane, where both nanoholes and interlayer pores are shown. The nanopores functions as a molecular sieve and the rejection of molecules is entirely based on the

relative size between the molecules and the nanopores. Nanoholes through the sheets can either exist as defects or be created by electron beam radiation, oxidative etching and plasma treatment amongst others. Interlayer poresize is highly controllable and can be adjusted at Angstrom level by inserting cations of different sizes into the interlayer of the material [11]. The other mechanism affecting the separation and permeation properties of a 2D membrane is intermolecular interactions between membrane material and the passing ions. Interactions such as hydrogen bonding, electrostatic interactions, local dipole interactions and Van der Waals interactions have a large influence on the membrane performance. [14]

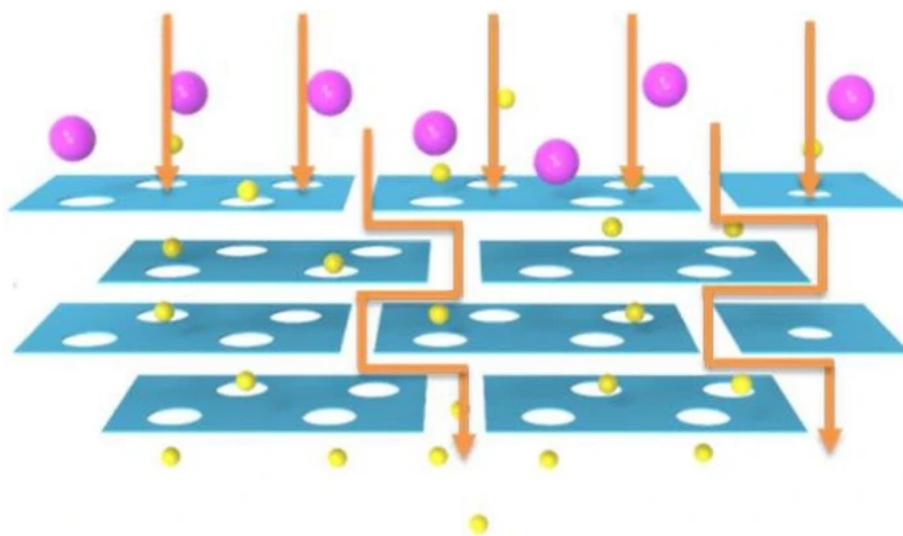


**Figure 2.6:** Structural representation of a 2D membrane. Both nanoholes and interlayer nanopores are present in this model. The purple dots represent pollutant molecules and the yellow dots represent water molecules. The arrows indicate fluid paths and entrance points. Modified from [11].

The use of 2D materials for membrane application has shown great potential, however, some challenges still remain. One of these challenges is swelling of the 2D materials that occurs when the 2D membrane is introduced to an aqueous environment [14]. Swelling is a phenomenon where water or other molecules enter the interlayer space between the 2D sheets causing the interlayer distance to increase. The molecules entering the interlayer can either hydrate or ion exchange with the existing interlayer molecules. An increment in interlayer spacing will affect selectivity, allowing more and bigger molecules to pass through the membrane and furthermore affect the stability of the membrane. Even though the interlayer is highly controllable when fabricating the membrane, it remains susceptible to swelling when applied in aqueous medium. A goal for future

2D membranes is to reduce or eliminate the swelling effect which would lead to more stable and selective membranes. [11]

### 2.3.1 Fabrication methods

2D Membranes can be fabricated by many different methods such as vacuum filtration, pressure assisted filtration, spin coating, dip coating and drop casting. All the mentioned methods produce thin 2D material layers and can easily be produced in a laboratory setting. Up-scaling can, on the other hand, be a challenging task where some methods are more suited for industrial productions than others. [39]

#### Vacuum filtration

Vacuum filtration is a simple method that involves passing a diluted dispersion of the 2D material through a filter substrate. The 2D material will either form a removable free standing membrane or stick to the filter through strong physical attachment caused by the vacuum pressure [39]. The method is highly suited for fabrication of hybrid membranes as several components can be added to the dispersion.

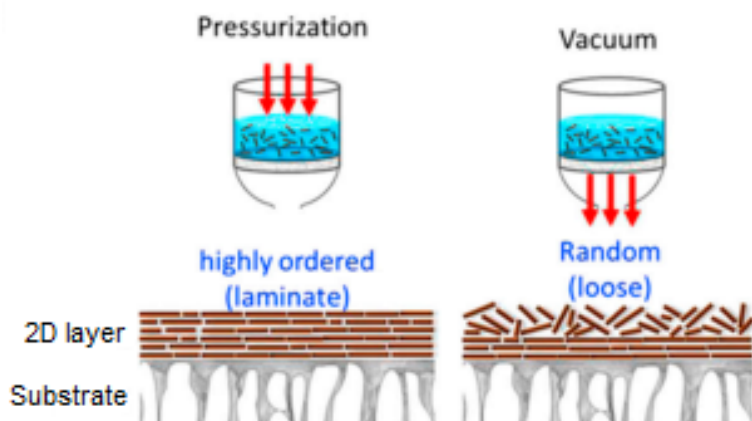


**Figure 2.7:** Stacking order of pressure assisted filtration and vacuum filtration. Modified from [39].

For example, when making a catalytic membrane both catalyst, 2D material and a binding component could be dispersed all together and further filtrated to form the hybrid membrane. Membrane thickness is easy to control as it is based on the concentration of 2D material in the dispersion [40].

However, thicker membranes takes longer time to prepare and may be less ordered in the upper region, as the vacuum pressure is strongest at the surface of the substrate [41]. Another drawback of the method is a high usage of solvents.

### **Pressure assisted filtration**

Pressure assisted filtration is very similar to vacuum filtration and shares many of the same characteristics. The main difference is that a positive pressure is applied to the dispersion that forces the dispersion through the filter, as illustrated in Figure 2.7. A more ordered 2D layer is formed by this method as the positive pressure is evenly distributed throughout the whole dispersion compared to vacuum filtration, where the vacuum pressure is strongest at the surface of the substrate [42]. The difference between an ordered and loose stacking is quite evident when examining the thickness of the produced membrane. For example, Tsou et al. [42] reported a reduction in membrane thickness from 384nm to 231nm, when comparing the two methods with similar GO dispersions.

### **Spin coating**

Spin coating makes use of a rotating disc where a 2D material dispersion is added onto the disc drop-wise. Centrifugal force from rotation causes the GO dispersion to align and spread evenly on top of the disc. The method is widely used in a laboratory setting and has successfully produced ultra-thin and well aligned GO coatings. GO membranes formed by this method has shown great potential in both gas- and liquid separations. However, the method is only suited for smooth substrate surfaces and flat shaped substrates. [39]

### **Dip coating**

The fabrication method of dip coating is a very intuitive and simple method, and is suited for a wide variety of substrate shapes. A substrate is immersed in a 2D material dispersion and allowed to soak. The 2D material will attach onto the substrate surface and form a thin membrane layer. The layer thickness can be controlled by a number of factors such as removal speed of the substrate, dispersion concentration and operating temperature. In effort to form a well aligned and uniform membrane layer, one must control the process carefully [39]. Zhang et al. [43] successfully synthesized hollow fiber GO membranes by dip coating and found that the substrate's removal speed from the GO dispersion was extremely important in order to form a uniform membrane layer. Another approach of ensuring a well aligned layer, is to functionalize the substrate beforehand

making the 2D material bind to the substrate covalently [44].

## 3 Materials & methods

### 3.1 Materials

The materials used in this work was either bought commercially or synthesized from commercially available precursors. GO and TiO<sub>2</sub> were bought commercially, GO as 10% w/w paste in water and TiO<sub>2</sub> as nano-sized powder. MnO<sub>2</sub> and MXene was synthesized from precursors. Table 3.1 shows all chemicals and compounds used for this project.

**Table 3.1:** List of used chemicals and manufacturers.

Compound	CAS-no.	Manufacturer	Purity	Note
TiO <sub>2</sub>	13463-67-7	Sigma-Aldrich	>99.5%	Mix of anatase and rutile (P25)
Graphene oxide	-	LayerOne	10%	Aq. paste
Ti <sub>3</sub> AlC <sub>2</sub>	196506-01-1	Sigma-Aldrich	>90%	MAX-phase material
LiF	7789-24-4	Thermo fisher	99.99%	-
MnCl <sub>2</sub> · 4H <sub>2</sub> O	13446-34-9	Sigma-Aldrich	>98%	-
(CH <sub>3</sub> ) <sub>4</sub> N(OH)	75-59-2	Sigma-Aldrich	25%	TMA·OH aq. solution
C <sub>6</sub> H <sub>5</sub> OH	108-95-2	Merck	>99%	Phenol
H <sub>2</sub> O <sub>2</sub>	7722-84-1	VWR chemicals	33%	-
HCl	7647-01-0	VWR chemicals	37%	-
KH <sub>2</sub> PO <sub>4</sub>	7778-77-0	VWR chemicals	>99%	-

#### 3.1.1 Synthesis of MnO<sub>2</sub>-nanosheets

Manganese dioxide nanosheets were synthesised by a bottom-up room-temperature synthesis. 4.3mL of 25wt% tetramethylammonium hydroxide solution (TMA·OH), 13.7mL DI water and 2mL 30wt% H<sub>2</sub>O<sub>2</sub> was mixed and added to 10mL 0.3M MnCl<sub>2</sub>·H<sub>2</sub>O solution. An immediate color change occurred when the two solutions were mixed, resulting in a dark brown solution. The solution was stirred for 36 hours, allowing the formation of MnO<sub>2</sub> particles. Finally, the solutions were centrifuged at 8000rpm for 20min. The precipitate was collected and washed three times with DI water and ethanol, separately.

### 3.1.2 Synthesis of $\text{Ti}_3\text{C}_2\text{T}_x$ MXene

MXene nanosheets were synthesised from a commercially available MAX-phase material with the molecular formula of  $\text{Ti}_3\text{AlC}_2$ . First, 1.6g LiF was slowly added to 20mL of 9M HCl in a teflon container, followed by stirring until LiF was completely dissolved. The solution container was placed in an ice bath and 1g  $\text{Ti}_3\text{AlC}_2$  was slowly and carefully added to the solution. An immediate exothermic reaction occurred when the powder was added to the solution, which was suppressed by being performed in an ice bath. The mixture was placed in a 55°C water bath and stirred for 48 hours, after the immediate exothermic reaction had occurred. Afterwards, the solution was centrifuged at 5000rpm for 5min and the precipitate was collected and washed with 1M HCl to remove excess LiF, followed by washing with DI water 8-10 times and until pH in the upper part of the solution was between 5-6. The precipitate was then transferred to 100mL deaerated DI water and sonicated for 2 hours in an ice bath. Both deaeration and sonication in ice was done to prevent oxidation of the material. The dispersion was then centrifuged at 3500rpm for 30 min. The supernatant was collected and freeze dried to obtain single- or few layered MXene.

### 3.1.3 2D material attached to $\text{TiO}_2$

Powder samples containing a mix of  $\text{TiO}_2$  and 2D materials were made to investigate the photocatalytic synergy between the materials. 0.5g of  $\text{TiO}_2$  was dispersed in 25mL DI-water and sonicated for 30min. 8mL of this dispersion was mixed with 1.6mL of 1000ppm GO,  $\text{MnO}_2$  and MXene dispersion, separately, to form dispersions containing 1% 2D material and 99% P25. The 2D dispersions were also sonicated for 30min prior to mixing with  $\text{TiO}_2$  dispersion. The dispersions were stirred for 1 hour before drying at 120°C in atmospheric air overnight. The obtained powders were mortared and later used for photocatalytic tests. For the photocatalytic tests, 0.05g of each powder was dispersed in 50 mL DI-water to make 1000ppm stock solutions, which were further diluted to 100ppm catalyst in 20ppm phenol solution.

## 3.2 Membrane fabrication

Membranes were fabricated using vacuum filtration method, see Figure 3.1 for the specific equipment. Stock dispersions of 1000ppm GO, MXene, MnO<sub>2</sub> and TiO<sub>2</sub> were made in DI-water, separately, and further diluted in 50mL dispersions used for membrane fabrication. The stock dispersions were sonicated for 1 hour before usage to promote a high degree of exfoliation. A typical dispersion for membrane fabrication contained 2-4mg material in 50mL DI-water and was sonicated for 30min prior to usage. Vacuum filtration were performed on PVDF, cellulose acetate and nylon filters with pore size of 0.45 $\mu$ m and 47mm in diameter. The PVDF and nylon filters were bought from Frisette and the cellulose acetate filter was bought from LabSolute. The filters serve as a support layer for the membrane. When performing vacuum filtration, the vacuum was retained for 30min after the solution had passed through the support to promote a strong physical attachment between the active layer and the support. All membranes were dried at ambient conditions overnight.

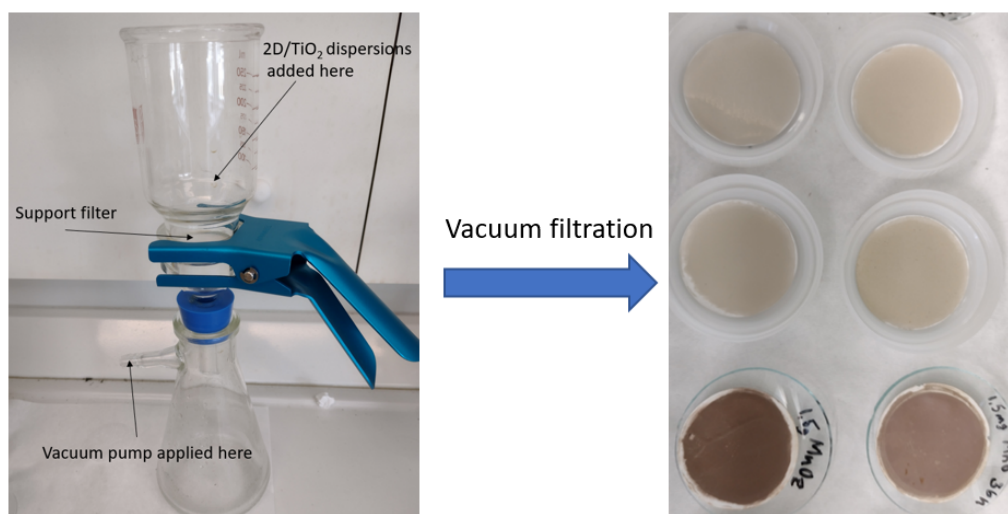


**Figure 3.1:** Equipment for membrane fabrication and examples of the resulting membranes.

## 3.3 Photocatalytic testing of dispersions

The photocatalytic capacities of TiO<sub>2</sub>, MXene, GO and MnO<sub>2</sub> dispersions were determined by making 50mL dispersions containing 20ppm dissolved phenol and 100ppm dispersed material. These

dispersions were transferred to a small reaction cell, see Figure 3.2. The quartz glass disc in the cell lid had a diameter of 47mm. Initially, the cell was covered in aluminum foil to avoid any illumination and the mixture was stirred for 60min to allow phenol adsorption on the particle surface. The aluminum foil was then removed to allow illumination of the cell and was kept at a constant temperature of 22°C by water cooling. Illumination was performed by a sun simulator calibrated to deliver 125mV. The dispersions were stirred during the whole experiment and samples were collected every 30min for a total time of 4 hours. All samples were analyzed by HPLC, using a C18 column, an injection volume of 80µL, a flowrate of 1mL/min and a static eluent composition of 70% 0.025M KH<sub>2</sub>PO<sub>4</sub> and 30% acetonitrile.

All 2D materials, TiO<sub>2</sub> and the 2D material attached to TiO<sub>2</sub> were tested this way. In addition, mixtures of 2D dispersion (17%) and TiO<sub>2</sub> dispersion (83%) were tested as well.

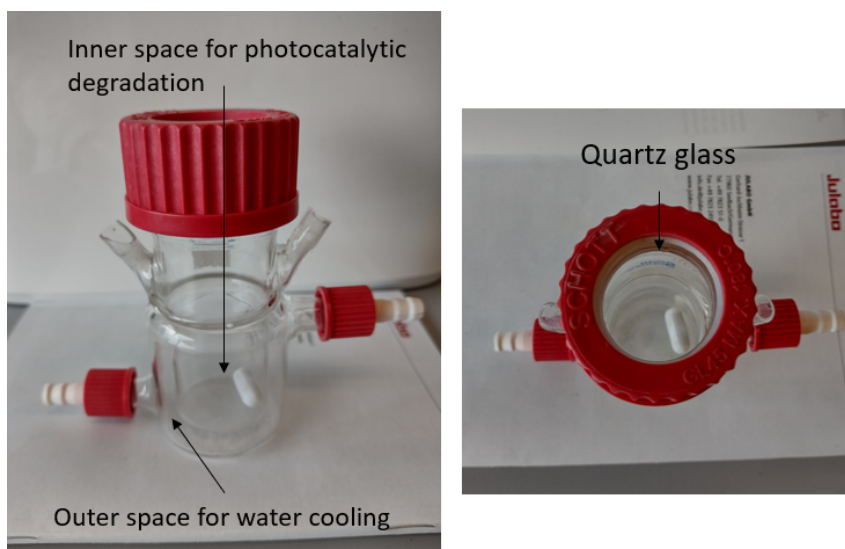


**Figure 3.2:** Equipment used for photocatalytic tests. Dispersions were added to the inner chamber, while the outer chamber was used for watercooling. Light was applied to the dispersions through the quartz glass disc incorporated in the lid.

### 3.4 Membrane filtration system

The equipment used to test membrane performance consisted of several different components, including a pump, UV-detector, membrane cell, lamp and a scale. Moreover, the system was set

up to provide a continuous cross-flow over the membrane surface. The whole system was highly customizable and flow channels such as permeate and retentate could easily be closed off in order to vary the operating conditions. Select parts of the system are shown in Figure 3.3. The light source provides wavelengths corresponding to sunlight and could be calibrated to deliver a variable intensity. For instance, the cell used for photocatalytic tests, Figure 3.2, has a different height than the membrane cell, Figure 3.3, and the light source was therefore calibrated to deliver equal intensities at different distances from the light source. The membrane cell was designed to fit a circular membrane with a diameter of 47mm and to allow illumination through a quartz glass disc at the active membrane area.

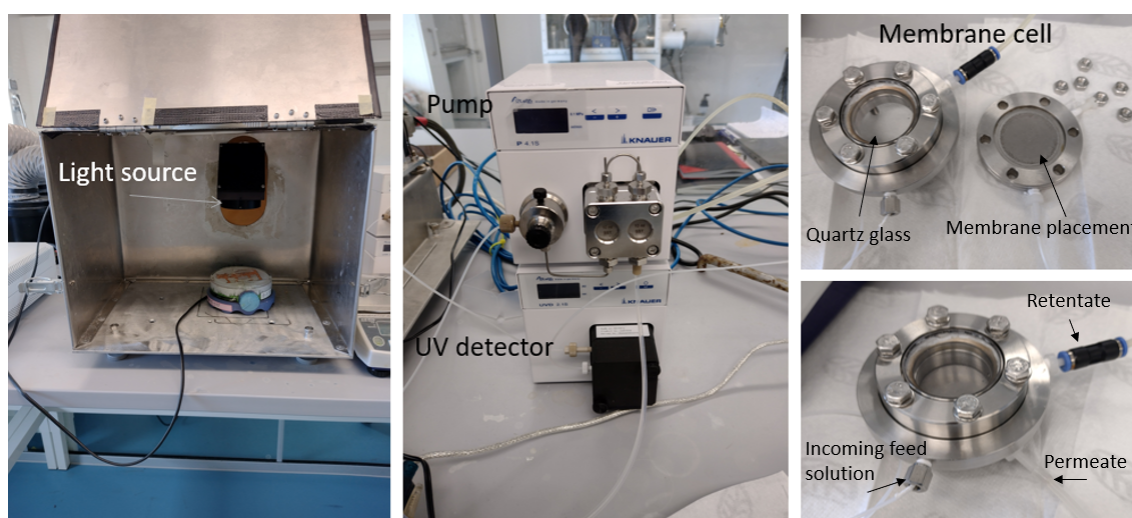


**Figure 3.3:** Equipment used for membrane and photocatalytic testing. The metal casing ensured dark conditions during experiments by blocking off any ambient sunlight and only allowing the light source to illuminate the cell.

A scheme of the complete setup is shown in Figure 3.4. The pump provided a constant flowrate of 5mL/min as well as an increase in pressure throughout the system. A pressure valve located after the membrane cell ensured that the pressure inside the membrane cell was adjustable and was further monitored by the pressure gauge. The light source was calibrated to deliver 125mV during experiments. The absorbance value of the retentate was analyzed during filtration at a static wavelength of 270nm. Permeate was collected during filtration and the mass flow was recorded. Analysis of permeate samples were performed by HPLC, not included in the current system. The pump, UV-detector and scale were all connected to a computer for both instrument control and automatic data acquisition. Pump and UV-detector had model name Azura P4.1S and Azura UVD

2.1S, respectively, and both instruments were produced by KNAUER.

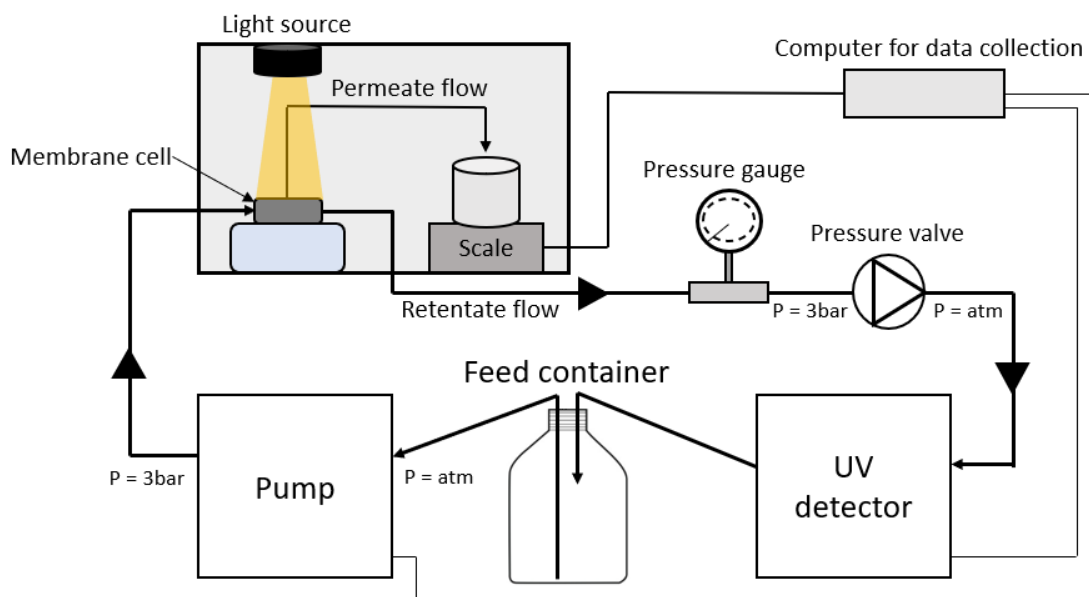


**Figure 3.4:** Scheme of the complete membrane filtration system.

### 3.4.1 Photocatalytic testing of membranes

Photocatalytic tests of the membranes were conducted to evaluate the photocatalytic properties of the materials when assembled in a membrane setting. The membranes were inserted in the membrane cell shown in Figure 3.3. However, the permeate flow was closed off allowing the feed solution to flow over the membrane for an extended time period. Additionally, the feed concentration and volume was not affected by permeation processes, thus isolating the photocatalytic effect of the membrane. The feed solution was 250mL of 20ppm phenol and was circulating over the membrane for 18hours, where the first 2 hours were in dark conditions. Simulated sunlight was applied after 2 hours and retained for the remaining 16 hours.

### 3.4.2 Membrane filtration

Filtration was performed in the membrane filtration system by inserting the membrane in the membrane cell, while having the feed solution flowing over the membrane for a variable time

and at a constant flow rate of 5.0mL/min. The permeate was collected and permeate flow was measured. Retentate was lead back into the feed container, as shown in Figure 3.4 The pressure in the membrane cell was kept constant at 3bar. Simulated sunlight was applied after 1 hour for membranes containing  $\text{TiO}_2$ , illuminating the membrane through the quartz glass disc. All filtration tests were measured during steady-state conditions, by flushing the system with the feed solution before initiating the experiments. The membrane was not exposed to sunlight during the flushing period, in order to deny photocatalysis and maintain original feed solution concentration.

## 4 Results & Discussion

### 4.1 Characterization of materials

#### 4.1.1 XRD phase analysis

XRD diffractograms of the materials used for membrane fabrication are shown in Figure 4.1. The  $\text{TiO}_2$  sample contains a mixture of anatase and rutile, which corresponds to the typical P25 composition [45]. The GO sample shows a large reflection around  $\approx 12^\circ$ , indicating exfoliated GO [30]. The synthesized MXene shows a large reflection at  $\approx 6^\circ$ , corresponding to the exfoliated MXene product [43]. Some of the original MAX-phase material still remains in the sample. A broad peak is present at  $\approx 9^\circ$  in the synthesized  $\text{MnO}_2$  sample, showing a similar diffractogram to the one found by Kai et al. [46] who identified the mineral to be monolayered or few layered  $\text{MnO}_2$  sheets.

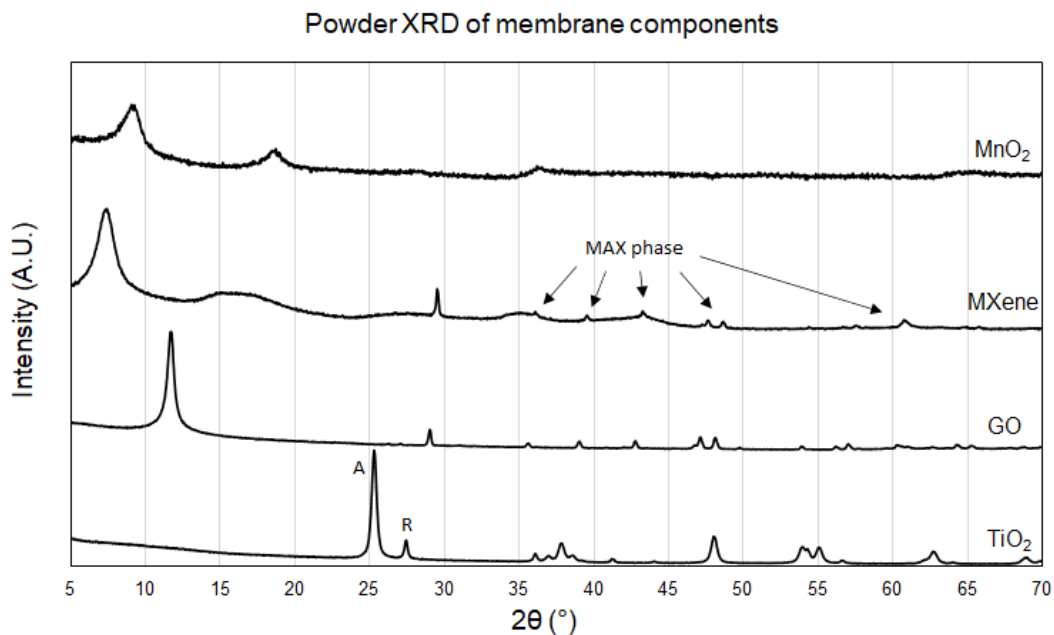


**Figure 4.1:** XRD diffractograms of the raw materials used for membrane fabrication. A corresponds to anatase. R corresponds to rutile.

The 1% 2D / 99% TiO<sub>2</sub> materials all show diffractograms similar to pure TiO<sub>2</sub>, Figure 4.2, with the exception of a small increase in the 5-15° area, which corresponds to the basal-reflections of the 2D materials (see Appendix 1 for a zoomed version of the 5-15° area). However, no other differences are observed, most likely due to the very small amount of 2D material compared to TiO<sub>2</sub>.

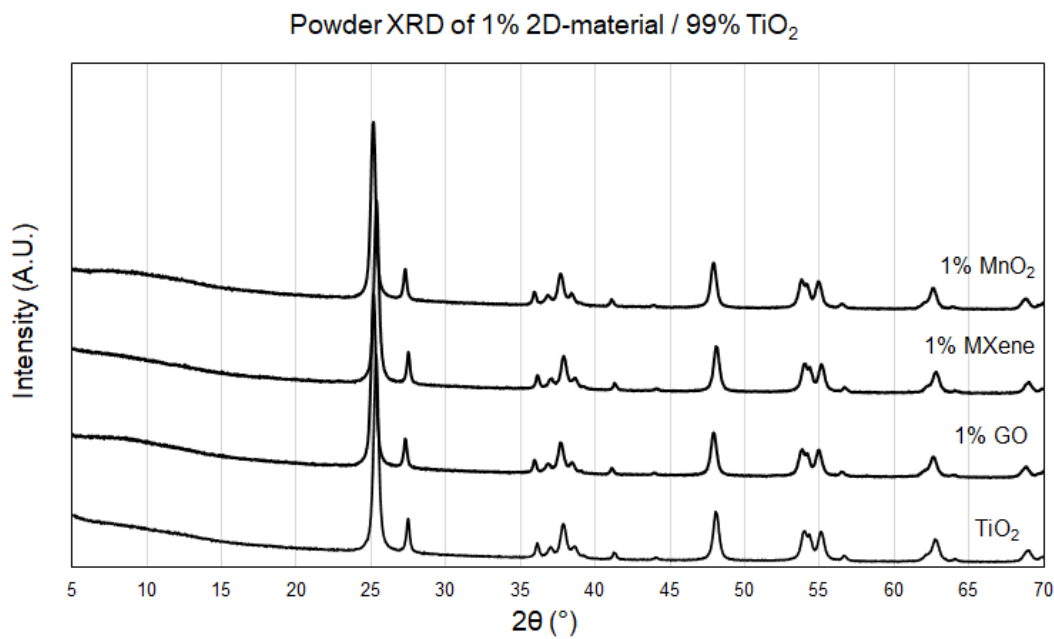


**Figure 4.2:** XRD diffractograms of the mixed 2D/TiO<sub>2</sub> materials.

## 4.2 Photocatalytic performance of dispersions

Photocatalytic performance of all used materials were investigated to highlight their ability to degrade phenol. The relative degradation of phenol ( $C/C_0$ ) over time is shown in Figure 4.3 for the various raw materials. Moreover, photolytic degradation of phenol is included as well.

Photolytic degradation of phenol in the absence of a catalyst showed a small reduction in concentration in the examined time span, degrading 0.5% of the total phenol content during 3 hours of illumination. For the case of the raw materials neither GO and MXene showed any sign of photocatalytic or adsorption behaviour, as the phenol concentration was more or less unchanged throughout the entirety of each experiment. MnO<sub>2</sub> did however show strong adsorption properties as the phenol concentration in solution decreased by  $\approx 7.5\%$  during dark conditions. The concen-

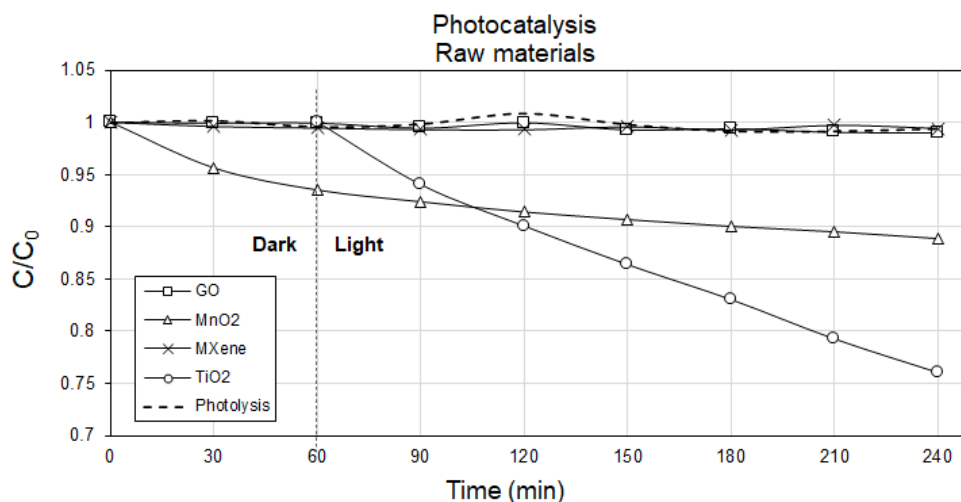


**Figure 4.3:** Photocatalytic degradation of phenol by raw materials used in this work. Phenol starting concentration was  $\approx 20$ ppm and catalyst loading was 100ppm in 50mL solutions. No illumination was applied in the first 60 minutes (dark). Illumination was applied at 60 minutes (light).

tration kept decreasing during light condition which could mean two things; either that the material exhibits photocatalytic properties or that the adsorption equilibrium had not been reached within the first hour in dark conditions.  $\text{TiO}_2$  show great photocatalytic properties, degrading roughly 25% of the total phenol content during 3 hours of illumination. Dispersions containing 17% 2D material and 83%  $\text{TiO}_2$  all showed photocatalytic properties, but at a decreased efficiency compared to  $\text{TiO}_2$  alone. Figures 4.4 (a) and (b) shows the phenol evolution for 17% and 1% dispersions, respectively. The dispersion containing  $\text{MnO}_2$  displayed the lowest efficiency, while MXene and GO dispersions showed a better photocatalytic efficiency. A reason why all dispersions showed worse efficiency than pure  $\text{TiO}_2$  could be due to the 2D materials obscuring the incoming light, as they heavily impact the turbidity and color of the solutions. Even formation of foam was observed for the MXene/ $\text{TiO}_2$  dispersion, which would screen off the incoming light. For the  $\text{MnO}_2$ / $\text{TiO}_2$  dispersion it was further observed that visible agglomerates formed during the experiment. Formation of agglomerates reduce the available surface area, leading to a reduction in the photocatalytic performance. The 1%-2D/ $\text{TiO}_2$  materials displayed better photocatalytic properties compared to their 17% counterparts, but did not yield improvements compared to pure  $\text{TiO}_2$ . The 1% materials share the same tendency as observed in the 17% mixtures, where the addition of 1%  $\text{MnO}_2$  yields the worst photocatalyst, followed by 1% MXene and then 1% GO.

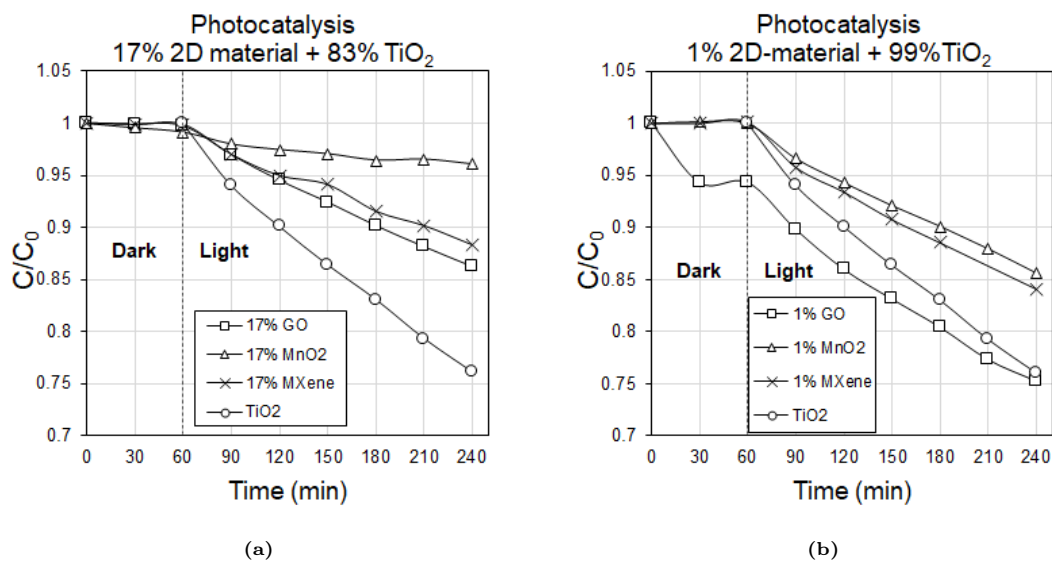


**Figure 4.4:** Photocatalytic degradation of 20 ppm phenol in 50mL 100ppm catalyst solution. (a) shows dispersions of 2D material and TiO<sub>2</sub> mixed in 20 ppm phenol. (b) shows the attached 2D/TiO<sub>2</sub> materials.

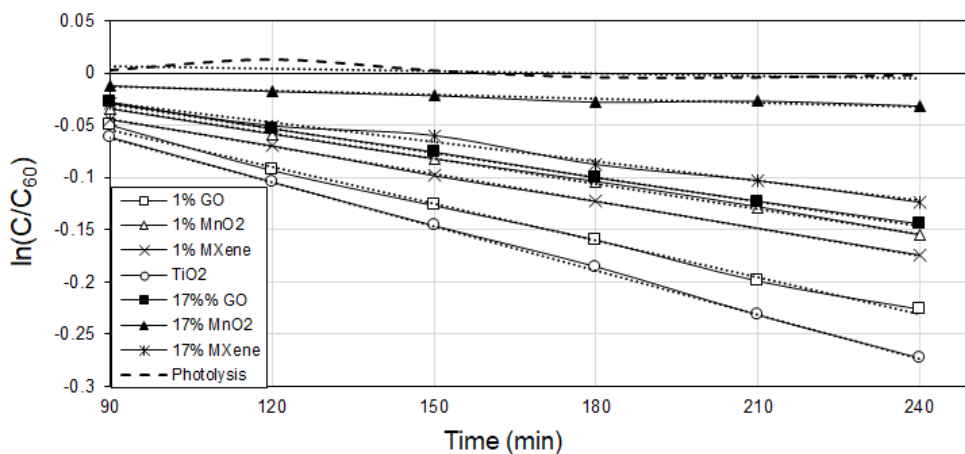


**Figure 4.5:** First-order reaction regression lines for degradation during illumination.

The 1%GO/TiO<sub>2</sub> material did decrease the phenol concentration more than pure TiO<sub>2</sub>, but is most likely caused by an improved adsorption capability as a large phenol reduction happened in dark conditions. The improved adsorption properties are unexpected, as GO by itself did not show signs of any adsorption, see Figure 4.3. In contrast, pure MnO<sub>2</sub> showed great adsorption capabilities for

phenol, but no improvement in adsorption was observed in the 1%MnO<sub>2</sub>/TiO<sub>2</sub> setting compared to pure TiO<sub>2</sub>.

All degradation experiments showed first-order reaction kinetics for the periods where illumination were applied. Figure 4.5 shows the first-order reaction representation of the various degradation experiments. The kinetic rate constants are listed in Table 4.1. From the rate constants, it is highly evident that pure TiO<sub>2</sub> is the better photocatalyst by a large margin, as the rate constant is  $\approx 20\%$  larger than the 1%GO rate constant, which was the second best photocatalyst in this work. However, several researchers [47] report a positive synergistic effect on the photocatalytic capacity when mixing TiO<sub>2</sub> and GO, but was not achieved with the current conditions.

**Table 4.1:** Table of first order kinetic constants for phenol degradation. All degradation experiments contained 100ppm material and 20ppm phenol in 50mL DI-water. Degradation percentages reported here exclude the drop in phenol concentration during dark conditions.

Content	Rate constant [ $s^{-1}$ ]	Degradation after 3h illumination [%]
Photolysis	$-0.77 * 10^{-4}$	0.18
TiO <sub>2</sub>	$-14.10 * 10^{-4}$	23.9
17% GO + 83% TiO <sub>2</sub>	$-7.79 * 10^{-4}$	13.5
17% MnO <sub>2</sub> + 83% TiO <sub>2</sub>	$-1.3 * 10^{-4}$	3.1
17% MXene + 83% TiO <sub>2</sub>	$-6.24 * 10^{-4}$	11.6
1% GO + 99% TiO <sub>2</sub>	$-11.77 * 10^{-4}$	20.2
1% MnO <sub>2</sub> + 99% TiO <sub>2</sub>	$-8.00 * 10^{-4}$	14.4
1% MXene + 99% TiO <sub>2</sub>	$-9.44 * 10^{-4}$	16.0

## 4.3 Membrane characterization

Membranes fabricated in this work showed very different appearances based on the type of support used. Using cellulose acetate support yielded poor adhesion between membrane material and the filter, where the membrane material would be flushed off during filtration or fall off when touched. Nylon filters had better adhesion, but produced membranes with very non-uniform appearances. Figure 4.6 shows some of the produced membranes and how the membrane material stuck to the support.

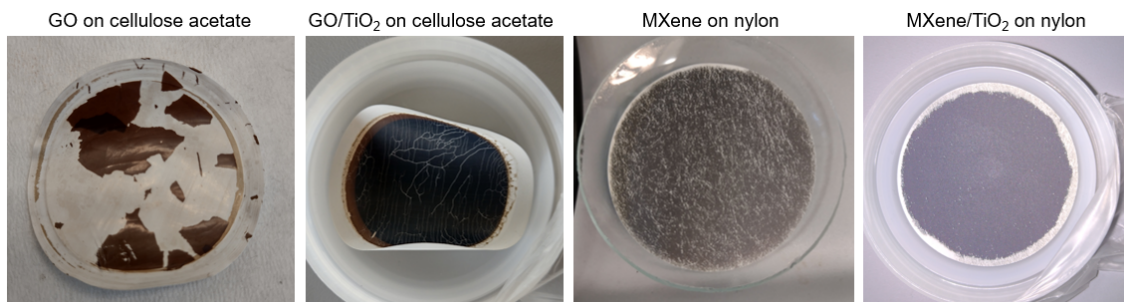


**Figure 4.6:** Pictures of cellulose acetate and nylon membranes.

PVDF did on the other hand show good adhesion and uniform appearance for GO and MXene, but did show a very poor uniformity for  $\text{MnO}_2$ . However, PVDF was the choice of support for the membranes reported in this work, as both cellulose acetate and nylon supports were considered worse options. Figure 4.7 shows membranes using PVDF supports.

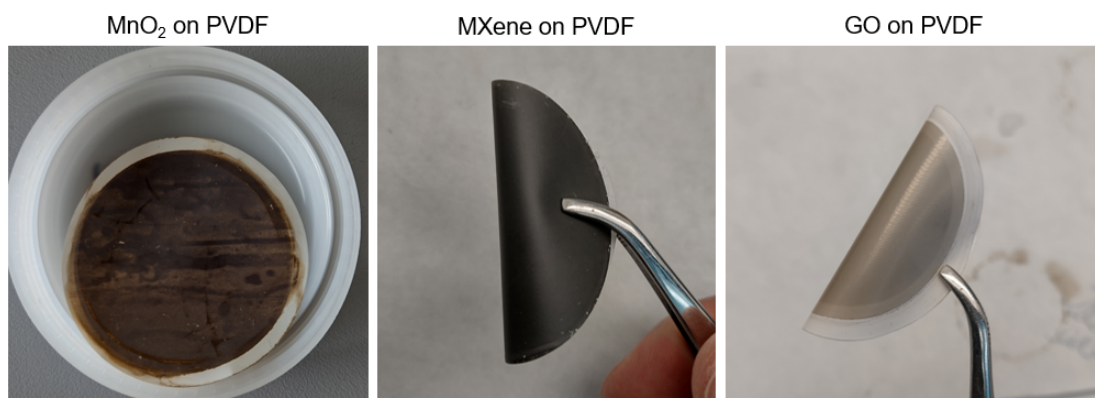


**Figure 4.7:** Pictures of PVDF membranes.

### 4.3.1 XRD analysis of membranes and supports

XRD analysis of the produced membranes, see Figure 4.8, show that the basal-reflection for both MXene and  $\text{MnO}_2$  change when vacuum filtered on top of the filter support. The basal-reflection in the GO membrane did not change significantly. Reflections originating from the support filter are also apparent in all the samples. The shift in interlayer spacing observed for the MXene sample indicate that the material is further exfoliated when sonicated before vacuum filtration. Furthermore, the material retains a narrow basal-reflection, indicating an ordered stacking structure. The GO-membrane has a very small shift for the basal-reflection, indicating that the material retains its original interlayer distance when applied in a membrane. The  $\text{MnO}_2$  membrane do not show a distinct peak for the original basal-reflection found in the powdered sample, but instead shows two regions around  $\approx 7^\circ$  and  $\approx 14^\circ$ . This could indicate that the  $\text{MnO}_2$  nanoparticles assembles in a more random stacking structure compared to the MXene and GO. When inspecting the appearance of the produced membranes, it is easily noticed that the MXene and GO membranes have uniform and smooth surfaces, whereas the  $\text{MnO}_2$  membranes show a very non-uniform surface with several bumps and varying color nuances.

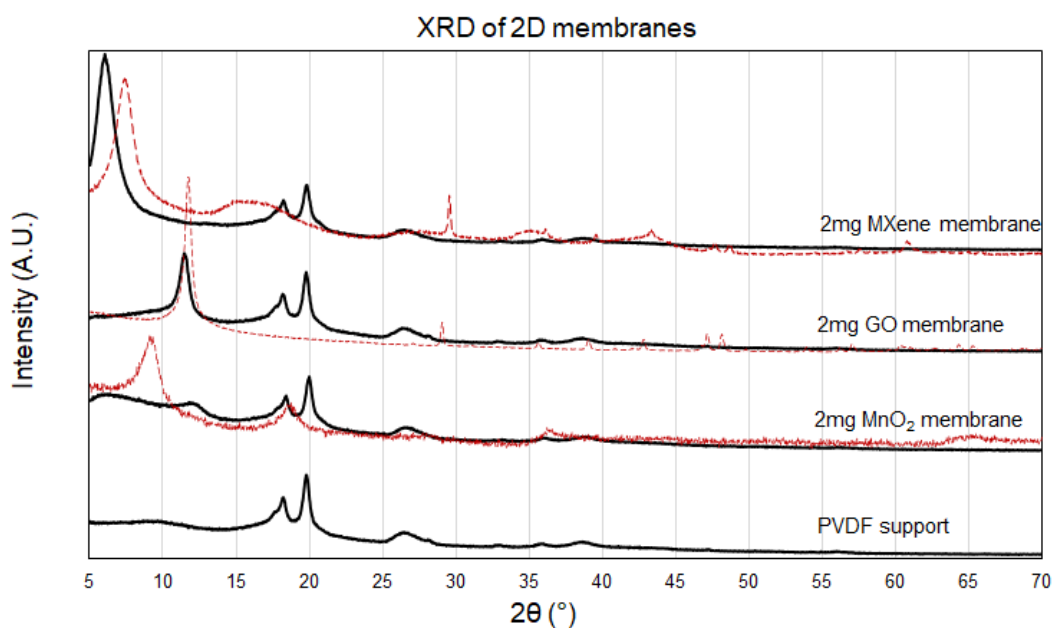


**Figure 4.8:** XRD measurement of 2D membranes. The red dotted line shows a powder/flake sample of the corresponding 2D material.

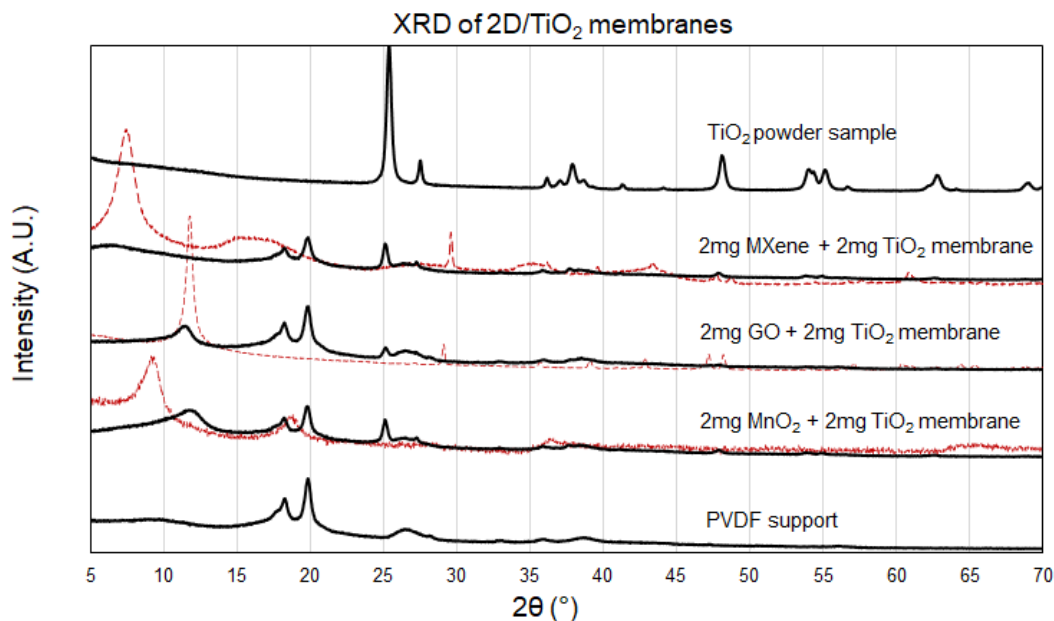


**Figure 4.9:** XRD measurement of 2D/TiO<sub>2</sub> membranes. The red dotted line shows a powder/flake sample of the corresponding 2D material.

**Table 4.2:** Basal-spacings for materials used for membrane fabrication and the resulting membranes. (\*) has two domains that could stem from the original basal-reflection.

	Basal-spacing [Å]	Basal-spacing [Å]	Basal-spacing [Å]
	Raw material	2mg membrane	2mg + 2mg TiO <sub>2</sub> membrane
GO	7.53	7.70	7.77
MXene	11.93	14.53	13.24
MnO <sub>2</sub>	9.60	13.75 and 7.33 (*)	7.56

Membranes consisting of both 2D material and TiO<sub>2</sub> are shown in Figure 4.9 and reveals that the addition of TiO<sub>2</sub> reduce the intensity of the basal-reflections for all membrane types. Moreover, the presence of the support filter and TiO<sub>2</sub> is apparent in every sample. Table 4.2 shows the basal-spacings for the various materials and membranes. The basal-spacing for GO remains more or less unchanged when applied together with TiO<sub>2</sub> for membrane application. Basal-spacing for MXene decreases in the presence of TiO<sub>2</sub>, which indicates that the TiO<sub>2</sub> particles have strong intermolecular interactions with the MXene material and constricts the sheets closer together.

However, the basal-reflection for the MXene/TiO<sub>2</sub> membrane is much broader and less intensive than for the pure MXene membrane, which indicate a more unordered structure. Comparing the pure MnO<sub>2</sub> and the MnO<sub>2</sub>/TiO<sub>2</sub> membranes it can further be seen that the reflection around  $\approx 7^\circ$  is not present in the MnO<sub>2</sub>/TiO<sub>2</sub> membrane. This observation can be explained by TiO<sub>2</sub> intercalation promoting a higher stacking order than MnO<sub>2</sub> alone. Additionally, the appearance of the MnO<sub>2</sub>/TiO<sub>2</sub> was visibly improved in regards to uniformity and surface smoothness.

### 4.3.2 Contact angle

Contact angle for the used supports and some select membranes were measured. The contact angle was found for a DI-water droplet and relates to the hydrophilicity of the membranes. Almost all supports and membranes showed a fast absorption of the water droplet and each contact angle reported here corresponds to the contact angle found after 0.5s of droplet-to-surface contact. Table 4.3 contains an overview of the measured contact angles for the supports and membranes.

**Table 4.3:** Contact angles measured for support filters and membranes.

Membrane content	Support type	Contact angle at 0.5s [°]
No coating	PVDF	32.79
No coating	Nylon	29.61
No coating	Cellulose acetate	45.19
2mg GO	PVDF	69.80
2mg MXene	PVDF	25.51
2mg MnO <sub>2</sub>	PVDF	Droplet absorbed too fast
2mg GO + 2mg TiO <sub>2</sub>	PVDF	Membrane bent when wetted
2mg MXene + 2mg TiO <sub>2</sub>	PVDF	13.91
2mg MnO <sub>2</sub> + 2mg TiO <sub>2</sub>	PVDF	11.01

The contact angles were in some cases not measurable as the membrane would absorb the water too quickly which caused the membrane to bend upwards, yielding an uneven surface and a misleading contact angle. This was the case for both the MnO<sub>2</sub> membrane and the GO/TiO<sub>2</sub> membrane.

The support filters show a varying degree of hydrophilicity, where the cellulose acetate filter is the most hydrophobic followed by PVDF and then nylon. This is highly correlated to the type and

abundance of surface groups present in each type of support filter. The GO/PVDF membrane yields a more hydrophobic surface, raising the contact angle of PVDF from  $32^\circ$  to  $70^\circ$ . This indicates a lower amount of hydrophilic surface groups in GO than in PVDF alone. The MXene active layer did, however, yield a much lower contact angle at  $26^\circ$  when coated on a PVDF support filter, indicating more hydrophilic surface groups present in MXene than in GO. The  $\text{MnO}_2$  membrane absorbed the water droplet before 0.5s had passed, showing an even higher hydrophilicity than MXene. Membranes consisting of both 2D material and  $\text{TiO}_2$  show very low contact angles at  $14^\circ$  and  $11^\circ$  for MXene/ $\text{TiO}_2$  and  $\text{MnO}_2/\text{TiO}_2$ , respectively. The low contact angles measured for the membranes partly consisting of  $\text{TiO}_2$  are highly related to  $-\text{OH}$  surface group that are dominating the  $\text{TiO}_2$  surface. The GO/ $\text{TiO}_2$  membrane started to bend upwards when introduced to the water droplet, which could be a consequence of swelling behaviour in the active layer.

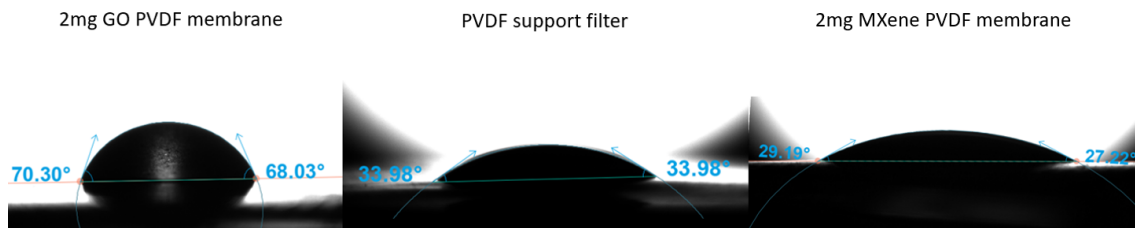


**Figure 4.10:** Some select pictures of contact angle measurements on membrane and support surface.

## 4.4 Membrane performance

The performance of the produced membranes have been divided into two separate sections, as several challenging issues occurred during the actual experiments. The initial objective was to measure photocatalytic degradation, permeation and selectivity all at the same time. However, the photocatalytic degradation proved to be extremely slow in the current membrane system. Moreover, the flux proved to be extremely high for the photocatalytic membranes. A small feed volume would be required to effectively assess the photocatalytic properties of the membrane, but a large feed volume would be needed to make the experiment last for an appropriate amount of time. The measurements of permeation and photocatalytic degradation were therefore separated. The permeate path was closed off when photocatalysis were measured and light was not applied when permeation and selectivity was measured.

### 4.4.1 Photocatalytic degradation

Photocatalytic degradation of some select membranes were performed over the course of 18hours with the permeate channel closed off. The samples were analyzed by both HPLC and the UV detector connected to the membrane system (see Figure 3.4). However, the two different analysis methods showed contradictory results, even though both instruments measured the absorbance at 270nm, Figure 4.11 and Table 4.4. The UV detector recorded a steady increase in absorbance for all membranes during the entire illumination period, whereas samples measured by HPLC showed a decrease in concentration. A most likely reason for the observed difference is leeching of membrane material into the feed solution. Suspended particles would absorb and scatter light in the UV detector and result in an increase in absorbance. Samples for HPLC analysis were passed through a  $0.45\mu\text{m}$  syringe filter during sampling, thus removing any leached membrane material from the sample. Moreover, only phenol was detected at 270nm in the HPLC analysis.

HPLC analyses revealed that phenol can be degraded by the membranes, but only to a small degree. During the 18 hour experiment, 8.6% of the 20ppm 250mL phenol solution was degraded when using the 1mg GO and 3mg  $\text{TiO}_2$  membrane. Membranes containing only 1mg  $\text{TiO}_2$  and 3mg 2D material showed much lower degradation percentages, ranging from 2.3% to 2.8%. This indicates a relation between the amount of  $\text{TiO}_2$  and degradation percentage. A larger amount of  $\text{TiO}_2$  is able to harvest more of the incoming light and form more radicals that can participate in

the degradation reaction. In addition, a larger available  $\text{TiO}_2$  surface area would provide more sites for phenol adsorption, also leading to a more efficient photocatalytic process. Degradation with membranes containing 3mg 2D material and 1mg  $\text{TiO}_2$ , show that MXene/ $\text{TiO}_2$  yields the highest degradation amount. This could indicate a better band-gap synergy between MXene and  $\text{TiO}_2$  compared to GO and  $\text{MnO}_2$ , however, this was not observed for the 1% 2D + 99%  $\text{TiO}_2$  materials when performing photocatalytic degradation using dispersions. A more thorough study of MXene and  $\text{TiO}_2$  in a membrane setting is needed to confirm the indication of band-gap synergy.

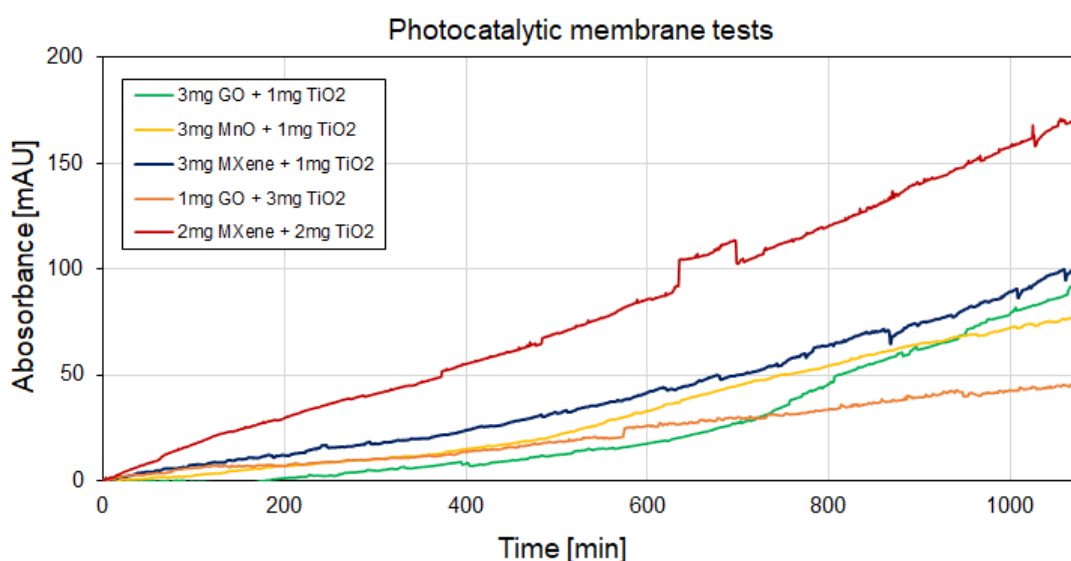


**Figure 4.11:** Absorbance evolution of the retentate stream measured by the UV detector connected to the filtration system. All measurements show the absorbance evolution starting at 0 mAU.

**Table 4.4:** Degradation of 20ppm phenol measured by HPLC compared to absorbance measured by UV detector. (\*) 50mL feed solution for this membrane, whereas 250 mL feed were used for other membranes.

Membrane content	Degradation at 18h [%]	
	Measured by HPLC	$\Delta$ Absorbance at 18h [mAU] Measured by UV-detector
3mg GO + 1mg $\text{TiO}_2$	2.3	92
3mg $\text{MnO}_2$ + 1mg $\text{TiO}_2$	2.3	78
3mg MXene + 1mg $\text{TiO}_2$	2.8	101
1mg GO + 3mg $\text{TiO}_2$	8.6	46
2mg MXene + 2mg $\text{TiO}_2$ (*)	8.8	171

#### 4.4.2 Permeation and selectivity

In general, most of the membranes produced in this work suffered from having very low rejection of phenol and a very high flux. A high flux is normally a good and sought-after property, however, for the current membrane filtration system a too high flux lead to several issues. One issue was that in the current cross-flow system, many membranes had such a high flux that the entire feed flow of 5mL/min passed the membrane. No pressure increase could be applied to the membrane cell as a consequence. Moreover, the permeability of those membrane could not be calculated accurately. Membranes that exhibited either too high permeation ( $>5\text{mL}/\text{min}$ ) or too low rejection ( $<5\%$ ) have been excluded from this report. For instance, all membranes containing  $\text{MnO}_2$  as 2D material did show too high permeation, where all the feed solution passed the membrane.

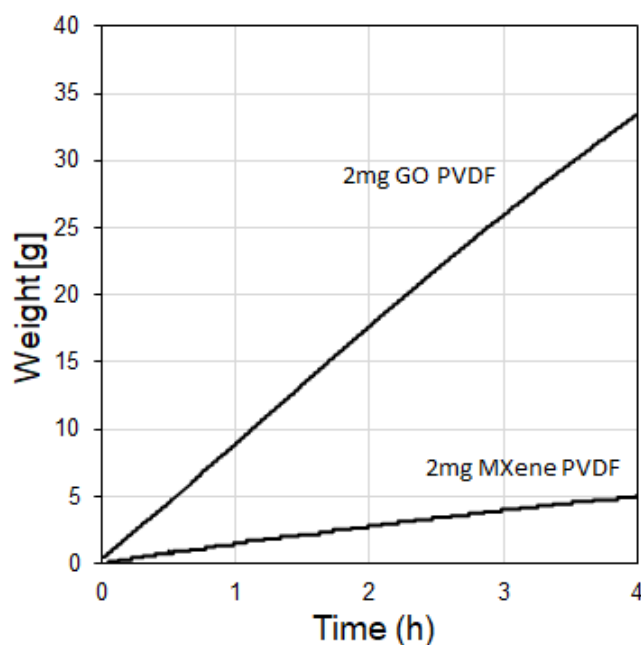


**Figure 4.12:** Mass flow during membrane filtration for 2mg GO and 2mg MXene PVDF membranes.

In addition to the very high fluxes, most  $\text{MnO}_2$  membranes showed poor rejection of phenol and, in some cases, did not reject any phenol. Membranes consisting of either 2mg GO or 2mg MXene as the only component in the active layer showed the best performances, rejecting 7.5% and 29.9% phenol, respectively. The flux for the 2mg GO membrane was  $5.06\text{Lm}^{-2}\text{bar}^{-1}\text{h}^{-1}$  and the flux from

the 2mg MXene membrane was  $0.75\text{Lm}^{-2}\text{bar}^{-1}\text{h}^{-1}$ . The MXene membrane performs much better than the GO membrane in terms of rejecting phenol, but provides a much lower water flux. The differences between the two membranes can be related to the pore structure of each material, where the MXene material must have smaller pores than GO. However, XRD analysis showed a larger interlayer distance for the MXene membrane compared to the GO membrane, where interlayer distance corresponds to interlayer pore size. Thus, a higher permeation and lower rejection was expected for the MXene membrane. A possible cause that explains this observation is swelling of the GO membrane that would increase the interlayer pore size, thus increasing water permeation and reducing selectivity. However, further analyses would be required to confirm this possibility. Microscopic cracks and defects could also explain the poor rejection of the GO membrane, as presence of these would increase permeation and reduce selectivity. Defects and cracks would also help to explain the extremely high fluxes for the excluded membranes, where the entire feed passed through the membrane. Additionally, this would also explain why the excluded membranes only rejected a very minimal amount of phenol.

## 5 Conclusion

Photocatalytic degradation of phenol using a  $\text{TiO}_2$  dispersion was proven possible, resulting in a 24% decrease in phenol concentration when degrading 20 ppm phenol with 100 ppm  $\text{TiO}_2$  in 50 mL DI-water. Degradation was determined to follow first order reaction kinetics. Moreover, addition of 2D material to the  $\text{TiO}_2$  dispersion during photocatalytic degradation, showed that GO had better synergy with  $\text{TiO}_2$  compared to MXene and  $\text{MnO}_2$ , but did not improve the photocatalytic degradation.

Membranes containing GO, MXene,  $\text{MnO}_2$  and  $\text{TiO}_2$  were successfully produced by vacuum filtration method, using PVDF filter as support. Deposition on the membrane surface affected the interlayer spacing for MXene and  $\text{MnO}_2$ , but not for GO. Contact angle measurements showed that the GO membrane surface had the lowest hydrophilicity follow by MXene and then  $\text{MnO}_2$ . 2D/ $\text{TiO}_2$  membranes showed small contact angles due to the presence of  $\text{TiO}_2$ .

A fully functional experimental filtration system was assembled and installed, but did show issues in regards to membrane leeching that would lead to inaccurate absorbance measurements. Phenol was successfully degraded by a membrane in a cross-flow filtration system by using a membrane containing both 2D material and  $\text{TiO}_2$  in the active layer. The degradation rate was much lower for the membrane compared to degradation using dispersions. The amount of  $\text{TiO}_2$  was found to heavily affect the degradation rate for membrane degradation, showing an increased degradation percentage at higher  $\text{TiO}_2$  content. A membrane consisting of only MXene showed the highest phenol rejection reported at 29.9% and flux at  $0.75\text{Lm}^{-2}\text{bar}^{-1}\text{h}^{-1}$ . A similar GO membrane showed rejection at 7.5% and flux at  $5.06\text{Lm}^{-2}\text{bar}^{-1}\text{h}^{-1}$ . The usage of  $\text{MnO}_2$  as membrane material did not prove feasible in this work.

# Bibliography

- [1] Chella Santhosh, Venugopal Velmurugan, George Jacob, Soon Kwan Jeong, Andrews Nir-mala Grace, and Amit Bhatnagar. Role of nanomaterials in water treatment applications: A review. *Chemical Engineering Journal*, 306:1116–1137, 12 2016. ISSN 13858947. doi: 10.1016/j.cej.2016.08.053.
- [2] Simon N. Gosling and Nigel W. Arnell. A global assessment of the impact of climate change on water scarcity. *Climatic Change*, 134:371–385, 2 2016. ISSN 15731480. doi: 10.1007/s10584-013-0853-x.
- [3] Muntathir Alshabib and Sagheer A. Onaizi. A review on phenolic wastewater remediation using homogeneous and heterogeneous enzymatic processes: Current status and potential challenges. *Separation and Purification Technology*, 219:186–207, 7 2019. ISSN 18733794. doi: 10.1016/j.seppur.2019.03.028.
- [4] Eva Eriksson, Anders Baun, Peter Steen Mikkelsen, and Anna Ledin. Risk assessment of xenobiotics in stormwater discharged to harrestrup Å, denmark. *Desalination*, 215:187–197, 9 2007. ISSN 00119164. doi: 10.1016/j.desal.2006.12.008.
- [5] Shohreh Mohammadi, Ali Kargari, Hamidreza Sanaeepur, Khalil Abbassian, Atefeh Na-jafi, and Elham Mofarrah. Phenol removal from industrial wastewaters: a short re-view. *Desalination and Water Treatment*, 53:2215–2234, 2 2015. ISSN 19443986. doi: 10.1080/19443994.2014.883327.
- [6] Laura G.Cordova Villegas, Neda Mashhadi, Miao Chen, Debjani Mukherjee, Keith E. Tay-lor, and Nihar Biswas. A short review of techniques for phenol removal from wastew-ater. *Current Pollution Reports*, 2:157–167, 9 2016. ISSN 21986592. doi: 10.1007/s40726-016-0035-3.
- [7] Xuemei Wang, Muxin Lu, Huan Wang, Yifei Pei, Honghong Rao, and Xinzhen Du. Three-dimensional graphene aerogels-mesoporous silica frameworks for superior adsorption capa-bility of phenols. *Separation and Purification Technology*, 153:7–13, 8 2015. ISSN 18733794. doi: 10.1016/j.seppur.2015.08.030.

- [8] Xuebing Hu, Yun Yu, Shuang Ren, Na Lin, Yongqing Wang, and Jianer Zhou. Highly efficient removal of phenol from aqueous solutions using graphene oxide/al<sub>2</sub>o<sub>3</sub> composite membrane. *Journal of Porous Materials*, 25:719–726, 6 2018. ISSN 15734854. doi: 10.1007/s10934-017-0485-z.
- [9] M. Kallel, C. Belaid, T. Mechichi, M. Ksibi, and B. Elleuch. Removal of organic load and phenolic compounds from olive mill wastewater by fenton oxidation with zero-valent iron. *Chemical Engineering Journal*, 150:391–395, 8 2009. ISSN 13858947. doi: 10.1016/j.cej.2009.01.017.
- [10] Kang Huang, Gongping Liu, Yueyun Lou, Ziyi Dong, Jie Shen, and Wanqin Jin. A graphene oxide membrane with highly selective molecular separation of aqueous organic solution. *Angewandte Chemie*, 126:7049–7052, 7 2014. doi: 10.1002/ange.201401061.
- [11] Wei Wang, Yanying Wei, Jiang Fan, Jiahao Cai, Zong Lu, Li Ding, and Haihui Wang. Recent progress of two-dimensional nanosheet membranes and composite membranes for separation applications. *Frontiers of Chemical Science and Engineering*, 15:793–819, 8 2021. ISSN 20950187. doi: 10.1007/s11705-020-2016-8.
- [12] Lloyd M. Robeson. The upper bound revisited. *Journal of Membrane Science*, 320:390–400, 7 2008. ISSN 03767388. doi: 10.1016/j.memsci.2008.04.030.
- [13] Huang Gao, Yaowu Hu, Yi Xuan, Ji Li, Yingling Yang, Ramses V. Martinez, Chunyu Li, Jian Luo, Minghao Qi, and Gary J. Cheng. Large-scale nanoshaping of ultrasmooth 3d crystalline metallic structures. *Science*, 346:1352–1356, 12 2014. ISSN 10959203. doi: 10.1126/science.1260139.
- [14] Gongping Liu and Wanqin Jin. Graphene oxide membrane for molecular separation: challenges and opportunities. *Science China Materials*, 61:1021–1026, 8 2018. ISSN 21994501. doi: 10.1007/s40843-018-9276-8.
- [15] Lingzhi Huang, Li Ding, and Haihui Wang. Mxene-based membranes for separation applications. *Small Science*, 1:2100013, 7 2021. ISSN 2688-4046. doi: 10.1002/smssc.202100013.
- [16] Caique Prado Machado de Oliveira, Inara Fernandes Farah, Konrad Koch, Jörg E. Drewes, Marcelo Machado Viana, and Míriam Cristina Santos Amaral. Tio<sub>2</sub>-graphene oxide nanocomposite membranes: A review, 1 2022. ISSN 18733794.

- [17] Katarzyna Janowska, Vittorio Boffa, Mads Koustrup Jørgensen, Cejna Anna Quist-Jensen, Fabien Hubac, Francesca Deganello, Fabrício E. Bortot Coelho, and Giuliana Magnacca. Thermocatalytic membrane distillation for clean water production. *npj Clean Water*, 3, 12 2020. ISSN 20597037. doi: 10.1038/s41545-020-00082-2.
- [18] Xiaogang Yang and Dunwei Wang. Photocatalysis: From fundamental principles to materials and applications. *ACS Applied Energy Materials*, 1:6657–6693, 12 2018. ISSN 25740962. doi: 10.1021/acsaem.8b01345.
- [19] Mohammed Muzibur Rahman. *Introductory Chapter: Fundamentals of Semiconductor Photocatalysis*. IntechOpen, 12 2019. doi: 10.5772/intechopen.89586.
- [20] Ewa Kowalska, Zhishun Wei, and Marcin Janczarek. 6 band-gap engineering of photocatalysts: Surface modification versus doping. 2018.
- [21] Saber Ahmed, M. G. Rasul, Wayde N. Martens, Richard Brown, and M. A. Hashib. Advances in heterogeneous photocatalytic degradation of phenols and dyes in wastewater: A review. *Water, Air, and Soil Pollution*, 215:3–29, 2 2011. ISSN 00496979. doi: 10.1007/s11270-010-0456-3.
- [22] S. K. Pardeshi and A. B. Patil. A simple route for photocatalytic degradation of phenol in aqueous zinc oxide suspension using solar energy. *Solar Energy*, 82:700–705, 2008. ISSN 0038092X. doi: 10.1016/j.solener.2008.02.007.
- [23] Gurudev Sujatha, Subramaniam Shanthakumar, and Fulvia Chiampo. Uv light-irradiated photocatalytic degradation of coffee processing wastewater using tio2 as a catalyst. *Environments - MDPI*, 7:1–13, 6 2020. ISSN 20763298. doi: 10.3390/environments7060047.
- [24] David F Ollis and Ezio Pelizzetti. Photocatalyzed destruction of water contaminants. *Environmental Science and Technology*, 25:99–114, 1991.
- [25] A A Adesina. Industrial exploitation of photocatalysis: progress, perspectives and prospects. *Catalysis Surveys*, 8:265–273, 2004.
- [26] Saber Ahmed, M. G. Rasul, Wayde N. Martens, R. Brown, and M. A. Hashib. Heterogeneous photocatalytic degradation of phenols in wastewater: A review on current status and developments. *Desalination*, 261:3–18, 2010. ISSN 00119164. doi: 10.1016/j.desal.2010.04.062.

- [27] Zhi-Hao Yuan, Jun-Hui Jia, and Li-De Zhang. Materials science communication influence of co-doping of zn(ii) + fe(iii) on the photocatalytic activity of tio 2 for phenol degradation. *Materials Chemistry and Physics*, 73:323–326, 2002.
- [28] Jianghao Wang, Guangshe Li, and Liping Li. Synthesis strategies about 2d materials, 8 2016.
- [29] William S Hummers and Richard E Offeman. Preparation of graphitic oxide. 1958.
- [30] Elvin Aliyev, Volkan Filiz, Muntazim M. Khan, Young Joo Lee, Clarissa Abetz, and Volker Abetz. Structural characterization of graphene oxide: Surface functional groups and fractionated oxidative debris. *Nanomaterials*, 9, 8 2019. ISSN 20794991. doi: 10.3390/nano9081180.
- [31] Andrew T. Smith, Anna Marie LaChance, Songshan Zeng, Bin Liu, and Luyi Sun. Synthesis, properties, and applications of graphene oxide/reduced graphene oxide and their nanocomposites. *Nano Materials Science*, 1:31–47, 3 2019. ISSN 25899651. doi: 10.1016/j.nanoms.2019.02.004.
- [32] Huitao Yu, Bangwen Zhang, Chaoke Bulin, Ruihong Li, and Ruiguang Xing. High-efficient synthesis of graphene oxide based on improved hummers method. *Scientific Reports*, 6, 11 2016. ISSN 20452322. doi: 10.1038/srep36143.
- [33] Yoshitomo Omomo, Takayoshi Sasaki, Lianzhou Wang, and Mamoru Watanabe. Redoxable nanosheet crystallites of mno2 derived via delamination of a layered manganese oxide. *Journal of the American Chemical Society*, 125:3568–3575, 3 2003. ISSN 00027863. doi: 10.1021/ja021364p.
- [34] Muyu Wu, Pingfu Hou, Lina Dong, Lulu Cai, Zhudian Chen, Mingming Zhao, and Jingjing Li. Manganese dioxide nanosheets: From preparation to biomedical applications, 2019. ISSN 11782013.
- [35] Li Ding, Libo Li, Yanchang Liu, Yi Wu, Zong Lu, Junjie Deng, Yanying Wei, Jürgen Caro, and Haihui Wang. Effective ion sieving with ti3c2tx mxene membranes for production of drinking water from seawater. *Nature Sustainability*, 3:296–302, 4 2020. ISSN 23989629. doi: 10.1038/s41893-020-0474-0.

- [36] Tian Zhang, Limei Pan, Huan Tang, Fei Du, Yanhua Guo, Tai Qiu, and Jian Yang. Synthesis of two-dimensional  $\text{Ti}_3\text{C}_2\text{TxMXene}$  using  $\text{HCl}+\text{LiF}$  etchant: Enhanced exfoliation and delamination. *Journal of Alloys and Compounds*, 695:818–826, 2017. ISSN 09258388. doi: 10.1016/j.jallcom.2016.10.127.
- [37] 2dsemiconductors. [www.2dsemiconductors.com](http://www.2dsemiconductors.com). URL <https://www.2dsemiconductors.com/MAXeneMXene/>.
- [38] Lingzhi Huang, Li Ding, and Haihui Wang. Mxene-based membranes for separation applications. *Small Science*, 1:2100013, 7 2021. ISSN 2688-4046. doi: 10.1002/smssc.202100013.
- [39] Ohchan Kwon, Yunkyoo Choi, Eunji Choi, Minsu Kim, Yun Chul Woo, and Dae Woo Kim. Fabrication techniques for graphene oxide-based molecular separation membranes: Towards industrial application. *Nanomaterials*, 11:1–15, 3 2021. ISSN 20794991. doi: 10.3390/nano11030757.
- [40] Dmitriy A. Dikin, Sasha Stankovich, Eric J. Zimney, Richard D. Piner, Geoffrey H.B. Dommett, Guennadi Evmenenko, Sonbinh T. Nguyen, and Rodney S. Ruoff. Preparation and characterization of graphene oxide paper. *Nature*, 448:457–460, 7 2007. ISSN 00280836. doi: 10.1038/nature06016.
- [41] Chi Hui Tsou, Quan Fu An, Shen Chuan Lo, Manuel De Guzman, Wei Song Hung, Chien Chieh Hu, Kueir Rarn Lee, and Juin Yih Lai. Effect of microstructure of graphene oxide fabricated through different self-assembly techniques on 1-butanol dehydration. *Journal of Membrane Science*, 477:93–100, 3 2015. ISSN 18733123. doi: 10.1016/j.memsci.2014.12.039.
- [42] Chi Hui Tsou, Quan Fu An, Shen Chuan Lo, Manuel De Guzman, Wei Song Hung, Chien Chieh Hu, Kueir Rarn Lee, and Juin Yih Lai. Effect of microstructure of graphene oxide fabricated through different self-assembly techniques on 1-butanol dehydration. *Journal of Membrane Science*, 477:93–100, 3 2015. ISSN 18733123. doi: 10.1016/j.memsci.2014.12.039.
- [43] Yatao Zhang, Qin Shen, Jingwei Hou, Putu Doddy Sutrisna, and Vicki Chen. Shear-aligned graphene oxide laminate/pebax ultrathin composite hollow fiber membranes using a facile dip-coating approach. *Journal of Materials Chemistry A*, 5:7732–7737, 2017. ISSN 20507496. doi: 10.1039/c6ta10395b.

- [44] Yingying Yin, Hui Li, Lei Zhu, Tianchao Guo, Xiao Li, Wei Xing, and Qingzhong Xue. A durable mesh decorated with polydopamine/graphene oxide for highly efficient oil/water mixture separation. *Applied Surface Science*, 479:351–359, 6 2019. ISSN 01694332. doi: 10.1016/j.apsusc.2019.01.118.
- [45] M. Rejek, J. Grzechulska-Damszel, and B. Schmidt. Synthesis, characterization, and evaluation of degussa p25/chitosan composites for the photocatalytic removal of sertraline and acid red 18 from water. *Journal of Polymers and the Environment*, 29:3660–3667, 11 2021. ISSN 15728919. doi: 10.1007/s10924-021-02138-x.
- [46] Kazuya Kai, Yukihiro Yoshida, Hiroshi Kageyama, Gunzi Saito, Tetsuo Ishigaki, Yu Furukawa, and Jun Kawamata. Room-temperature synthesis of manganese oxide monosheets. *Journal of the American Chemical Society*, 130:15938–15943, 11 2008. ISSN 00027863. doi: 10.1021/ja804503f.
- [47] Nisha T. Padmanabhan, Nishanth Thomas, Jesna Louis, Dhanu Treasa Mathew, Priyanka Ganguly, Honey John, and Suresh C. Pillai. Graphene coupled tio2 photocatalysts for environmental applications: A review. *Chemosphere*, 271, 5 2021. ISSN 18791298. doi: 10.1016/j.chemosphere.2020.129506.

# Appendix

# A Appendix 1

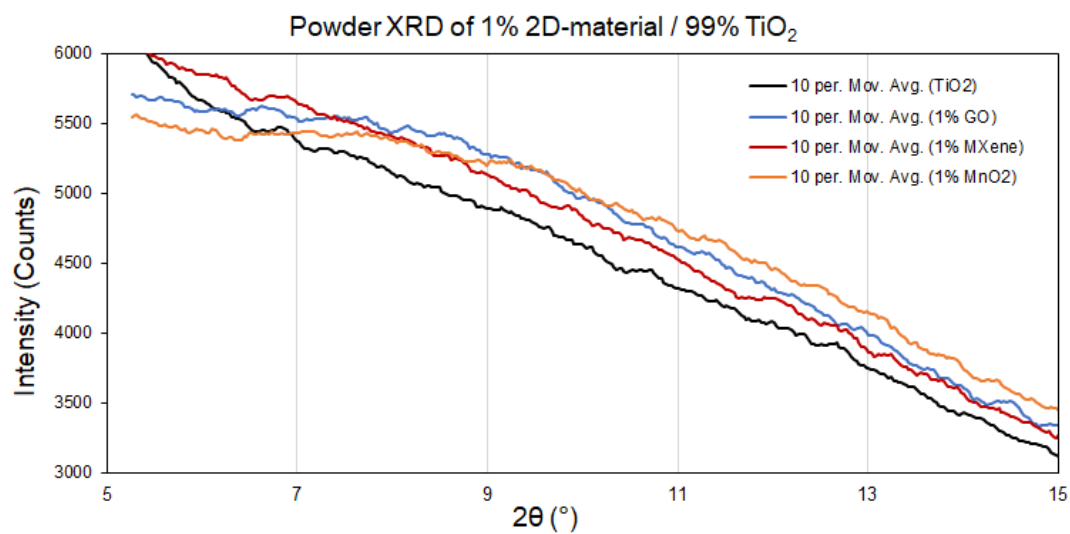


**Figure A.1:** XRD diffractograms of the mixed 2D/TiO<sub>2</sub> materials zoomed in on the 5-15° area using a moving average of 10 data points.